Power uprates
and plant life extension

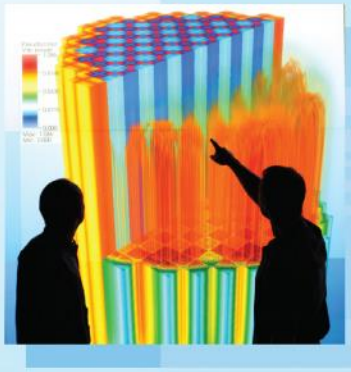

Engineering design
and analysis

Science-enabling
high performance
computing

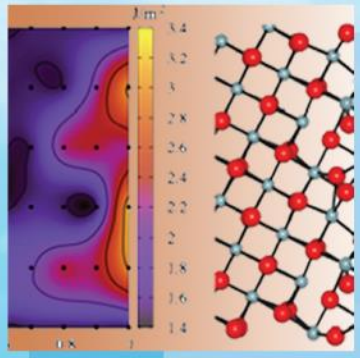

Fundamental science

Plant operational data

Consortium for Advanced Simulation of LWRs

CILC Studies with Comparative Analysis to Existing Plants L2.MPO.P7.06

BRIAN KENDRICK
Los Alamos National Laboratory

VICTOR PETROV
DANIEL WALTER
ANNALISA MANERA
University of Michigan

U.S. DEPARTMENT OF ENERGY | Nuclear Energy

REVISION LOG

Revision	Date	Affected Pages	Revision Description
0	09/30/2013	All	Initial Issuance

Document pages that are:

Export Controlled _____ _____

IP/Proprietary/NDA Controlled _____ _____

Sensitive Controlled_____

Requested Distribution:

To:

CASL Senior Leader Team (SLT)

Extended Leadership Team (ELT)

Copy:

EXECUTIVE SUMMARY

This milestone is the first attempt to demonstrate and assess the ability of state-of-the-art high-fidelity computational tools to reproduce the complex patterns of CRUD deposits found on the surface of operating Pressurized Water Reactors (PWRs) fuel rods.

A fuel assembly of the Seabrook PWR was selected as the test problem. In Seabrook Cycle 5, CRUD induced power shift (CIPS) and localized corrosion (CILC) failures were observed. Measurements of the clad oxide thickness on both failed and non-failed rods are available, together with visual observations and the results from CRUD scrapes of peripheral rods.

A complete high fidelity simulation of CRUD deposition requires the coupling of a Computational Fluid Dynamics (CFD) code, a three-dimensional chemistry code and a neutron transport code. For this milestone, however, the coupled simulations were limited to CFD and chemistry, while the time-dependent pin power distributions were calculated by means of an off-line neutronics simulation. Even though the original milestone definition included only power profiles calculated with the Westinghouse Electric Company (WEC) neutron diffusion code ANC, additional simulations were performed with a neutron transport code, in order to investigate the effects of azimuthal changes in pin power distribution on CRUD deposition.

The simulations presented in this milestone have been carried out blindly, i.e. the experimental data have been made available to this milestone team after the simulations had been already completed.

In addition to the simulation of a Seabrook Cycle 5 fuel assembly, additional studies on a single fuel pin were performed in order to investigate the effect of selected physical phenomena and of the time-stepping of the numerical scheme for the coupling between CFD and chemistry.

CONTENTS

1 MILESTONE DESCRIPTION....11
1.1 Seabrook Cycle 5....11

2 TEST PROBLEMS AND SENSITIVITY STUDIES....14
2.1 Description of sensitivity studies....14
2.2 Problem Description – Seabrook 5x5 fuel assembly....14
2.2.1 STAR-CCM+ model....17
2.2.2 MAMBA model....21
2.2.3 Power distribution from ANC – no azimuthal variation (case 1a)....23
2.2.4 Power distribution from DeCART with azimuthal variation (case 2a)....24
2.3 Problem Description – Single Pin....26
2.3.1 STAR-CCM+ model....26
2.3.2 MAMBA model....27

3 TEST PROBLEMS AND SENSITIVITY STUDIES....28
3.1 RESULTS FOR SEABROOK 5x5 SUB-ASSEMBLY....28
3.1.1 STAR-CCM+/MAMBA simulation with ANC power distribution (case 1a)....28
3.1.2 STAR-CCM+/MAMBA with azimuthal power distribution (case 2a)....43
3.2 RESULTS FOR SINGLE PIN TEST PROBLEM....48
3.2.1 STAR-CCM+/MAMBA simulations with fixed time steps (case 1b)....48
3.2.2 Influence of turbulence model (case 2b)....49

4 CONCLUSIONS....53

5 REFERENCES....55

6 INITIAL COMPARISONS WITH THE SEABROOK CRUD DATA (submitted separately due to export control issues)

FIGURES

Figure 1: Seabrook Cycle 5 core configuration. Fuel assemblies containing failed pins are indicated with the red boxes. 12

Figure 2: Seabrook Cycle 5 reactor power and corresponding axial offset (top), coolant PH (bottom). 12

Figure 3: Boron and Lithium letdown curves (Seabrook cycle 5). 13

Figure 4: Nickel soluble and particulate concentration curves (Seabrook cycle 5). 13

Figure 5: Seabrook Cycle 5 Assembly G70. The 5x5 region selected for STAR-CCM+/MAMBA simulations is highlighted by the red squared region. 15

Figure 6: CAD for 5x5 grid spacer with mixing vanes. 16

Figure 7: Spacers geometry and dimensions in mm. 16

Figure 8: Geometry of mixing vanes with dimensions in mm. 16

Figure 9: Axial location of grid spacers (left) and adopted rod numbering (right). 17

Figure 10: Cross-section of the CFD computational mesh. 18

Figure 11: Detail of CFD computational mesh of mixing vanes. 18

Figure 12: Magnitude of the velocity field above a grid spacer. 19

Figure 13: Axial power distribution of G70 assembly at select burnup states. 23

Figure 15: Azimuthal power variation for pins surrounding guide tube, plane 12, 4 days. 25

Figure 16: Azimuthal power variation for pins 1, 8, and 9, plane 12, 4 days. 25

Figure 17: Pin cell model. 26

Figure 18: Grid spacer with mixing vanes (left) and boundary conditions and mesh (right). 27

Figure 19: MAMBA/STAR-CCM+ time stepping algorithm for single pin cell time stepping study. 28

Figure 20: Cladding temperature at 4 days (case 1a). 29

Figure 21: Cladding temperature at 261 days (case 1a). 29

Figure 23: CRUD thickness [microns] at 502 days (case 1a). 30

Figure 24: CRUD thermal resistance [m^2K/W] at 502 days (case 1a). 31

Figure 25: Turbulent kinetic energy at 502 days (case 1a). 31

Figure 26: Azimuthal distribution of cladding temperature for pin #8, spacer 1, at 4 days. 32

Figure 27: Azimuthal distribution of cladding temperature for pin #8, spacer1, at 261 days.....32

Figure 28: Azimuthal distribution of cladding temperature for pin #8, spacer1, at 502 days.....32

Figure 29: Axial location along grid spacer for azimuthal distributions of Figure 26 to Figure 28.....33

Figure 30: 5x5 pin designation with vanes orientation (same for grids 5, 6 & 7). 34

Figure 31: 3D top view of 3x3 surrounding the center guide tube at 502 days. 35

Figure 32: 3D face view of 3x3 at 502 days. 35

Figure 33: 3D face view of 3x3 at 502 days 36

Figure 34: Total CRUD mass on each pin vs time.....37

Figure 35: Maximum CRUD thickness on each pin vs time 37

Figure 36: 2D surface contour maps of the CRUD thickness (in microns at 502 days) – pins 7 to 9. The dashed vertical line in the middle panel shows the location of the 2D profile plot in Figure 39.....39

Figure 37: 2D surface contour maps of the CRUD thickness (in microns at 502 days) – pins 12 & 14. The dashed vertical line in the left panel shows the location of the 2D profile plot in Figure 40.....39

Figure 38: 2D surface contour maps of the CRUD thickness (in microns at 502 days) – pins 17 to 19.....40

Figure 39: 2D CRUD profiles at 502 days for pin #8. 40

Figure 40: 2D CRUD profiles at 502 days for pin #12. 41

Figure 41: 2D surface contour maps of the boiling chimney mass evaporation flux [kg/s m^2] at 209 days – pins 7 to 9.....41

Figure 42: 2D surface contour maps of the boiling chimney mass evaporation flux [kg/s m^2] at 209 days – pins 12 to 14.....42

Figure 43: 2D surface contour maps of the boiling chimney mass evaporation flux [kg/s m^2] at 209 days – pins 17 to 19.....42

Figure 44: Cladding temperature at 502 days (case 2a). 44

Figure 45: CRUD thickness [microns] at 502 days (case 2a).....44

Figure 46: Azimuthal distribution of cladding temperature for pin #8, spacer 1, at 502 days. Solid lines (case 2a), dashed lines (case 1a). 45

Figure 47: 2D surface contour maps of the CRUD thickness (in microns at 502 days) for pin #8 with and without azimuthal power variations. 46

Figure 48: 2D surface contour maps of the CRUD thickness (in microns at 502 days) for pin #12 with and without azimuthal power variations. 46

Figure 49: Integral CRUD mass, maximum CRUD thickness and integral boron mass comparison of ANC and azimuthally varying ANC power simulations for pin 11 and 12. 47

Figure 50: Core total integral CRUD mass, maximum CRUD thickness and integral boron mass comparison of ANC and azimuthally varying ANC power simulations. 47

Figure 51: MAMBA/STAR-CCM+ time stepping algorithm for single pin cell time stepping study. 48

Figure 52: Integral CRUD mass, maximum CRUD thickness and integral boron mass for 50, 25, and 10 day MAMBA/STAR-CCM+ time steps (data exchanges). 48

Figure 53: Axial locations in the proximity of the mixing vanes. 49

Figure 54: Power density profile used for sensitivity study 2b. 50

Figure 55: Azimuthal variation of cladding temperature in proximity of grid spacer #3. 51

Figure 56: Azimuthal variation of turbulent kinetic energy in proximity of grid spacer #3. 51

Figure 57: Azimuthal variation of turbulent kinetic energy in proximity of grid spacer #358. 52

TABLES

Table 1 – Seabrook PWR main parameters.....13

Table 2 – Dimensions of fuel pins and guide tubes.....17

Table 3 –Summary of CFD mesh.....20

Table 4 – Thermo-physical properties of materials.....20

Table 5 – Fluid properties and UO2 thermal conductivity.....20

Table 6 – CFD mesh sensitivity study.....21

Table 7 – ANC burnup steps and relative power of G70 assembly.....23

Table 8 – STAR-CCM+ mesh information for single-pin model.....27

Table 9 – STAR-CCM+ mesh information for single-pin model.....50

ACRONYMS

1D	one-dimensional
3D	three-dimensional
AO	Axial offset
CASL	Consortium for Advanced Simulation of Light Water Reactors
CFD	computational fluid dynamics
CILC	CRUD induced localized corrosion
CIPS	CRUD induced power shift
DOE	U.S. Department of Energy
EFPD	Effective Full Power Days
HZP	Hot zero power
IFBA	Integral Fuel Burnable Absorber
LANL	Los Alamos National Laboratory
MPO	Materials Performance Optimization Focus Area
NDA	non-disclosure agreement
NPP	nuclear power plant
PWR	pressurized water reactor
Re	Reynolds number
STAR-CCM+	Simulation of Turbulence in Arbitrary Regions-Computational Continuum Mechanics
T-H	thermal-hydraulics
VERA	Virtual Environment for Reactor Applications
VI	VERA Integration
VIPRE	Versatile Internals and Component Program for Reactors
VIPRE-W	Westinghouse version of VIPRE
WEC	Westinghouse Electric Company

1 MILESTONE DESCRIPTION

This milestone is the first attempt to demonstrate and assess the ability of state-of-the-art high-fidelity computational tools to reproduce the complex patterns of CRUD deposits found on the surface of operating Pressurized Water Reactor (PWR) fuel rods.

A fuel assembly of the Seabrook PWR was selected as the test problem. In Seabrook Cycle 5, CRUD induced power shift (CIPS) and localized corrosion (CILC) failures were observed. Measurements of the clad oxide thickness on both failed and non-failed rods are available, together with visual observations and the results from CRUD scrapes of peripheral rods.

A complete high fidelity simulation of CRUD deposition requires the coupling of a Computational Fluid Dynamics (CFD) code, a three-dimensional chemistry code and a neutron transport code. For this milestone, however, the coupled simulations were limited to CFD and chemistry, while the time-dependent pin power distributions was calculated by means of an off-line neutronics simulation. Even though the original milestone definition included only power profiles calculated with the Westinghouse Electric Company (WEC) multi-dimensional nodal code ANC [1], additional simulations were performed with a neutron transport code, in order to investigate the effects of azimuthal changes in pin power distribution on CRUD deposition. The simulations presented in this milestone have been carried out blindly, i.e. the experimental data have been made available to this milestone team after the simulations had been already completed.

In addition to the simulation of a Seabrook Cycle 5 fuel assembly [2], additional studies on a single fuel pin were performed in order to investigate the effect of selected physical phenomena and of the time-stepping of the numerical scheme for the coupling between CFD and chemistry.

The scope of the present milestone was finalized at the end of June 2013. The ANC data were received the following July. Unfortunately, because of delays with the non-disclosure agreement (NDA) procedures, the report with the Seabrook geometry specifications and experimental data [2] was received on September 10th. By this time, it was realized that the orientation of some of the grid spacer mixing vanes was represented incorrectly in the CFD model. Also, it was realized that the axial position of the bottom of the rods was shifted slightly. Thus, additional simulations with the corrected geometry could not be performed in the short time frame available to complete this report; the incorrect orientation of some of the mixing vanes has highlighted some interesting effects on the CRUD deposition patterns. These results are discussed in detail in chapters 3.1 and 6.

1.1 Seabrook Cycle 5

Seabrook is a Westinghouse design 4-loop PWR. Compared with previous cycles, Cycle 5 (December 1995 – May 1997) consisted of a more aggressive core design, with increased cycle length and increased rod powers.

At 10,000 MWD/MTU, or 260 effective full-power days (EFPD), considerable CIPS became apparent, with a maximum axial offset (AO) of about -3.3 %. Fuel failures started to be detected at about 350 EFPD. In particular five failed rods were observed in four distinct fuel assemblies. The assemblies containing the failed rods were part of a symmetric group of a total of twelve

assemblies characterized by the highest powers for the entire cycle. All five failed rods contained Integral Fuel Burnable Absorber (IFBA) and were adjacent to guide thimbles.

A sketch of the core is presented in Figure 1, while the main plant parameters are reported in Table 1. The location of the fuel assemblies containing failed fuel rods are highlighted in red. The core power and coolant PH are shown in Figure 2. Boron and lithium letdown curves are reported in Figure 3, while the nickel soluble and particulate concentration during the cycle 5 length are reported in Figure 4.

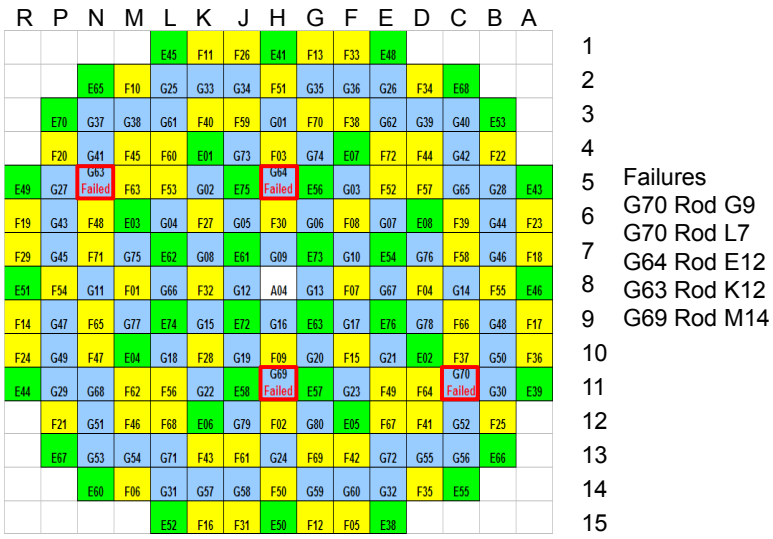

Figure 1: Seabrook Cycle 5 core configuration. Fuel assemblies containing failed pins are indicated with the red boxes.

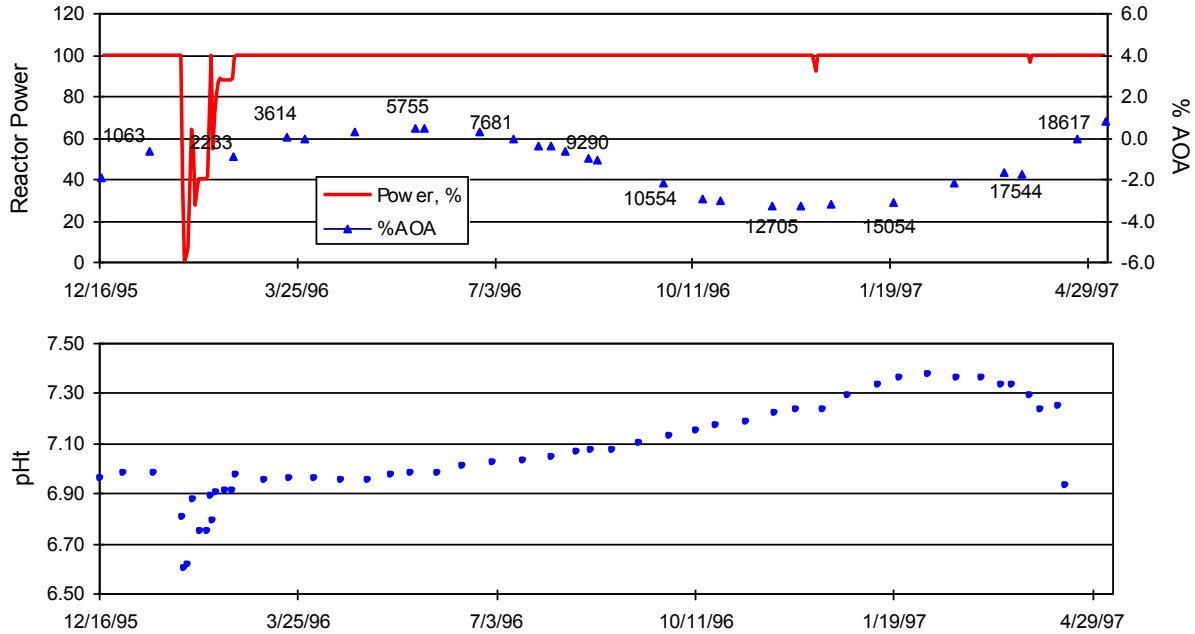

Figure 2: Seabrook Cycle 5 reactor power and corresponding axial offset (top), coolant PH (bottom).

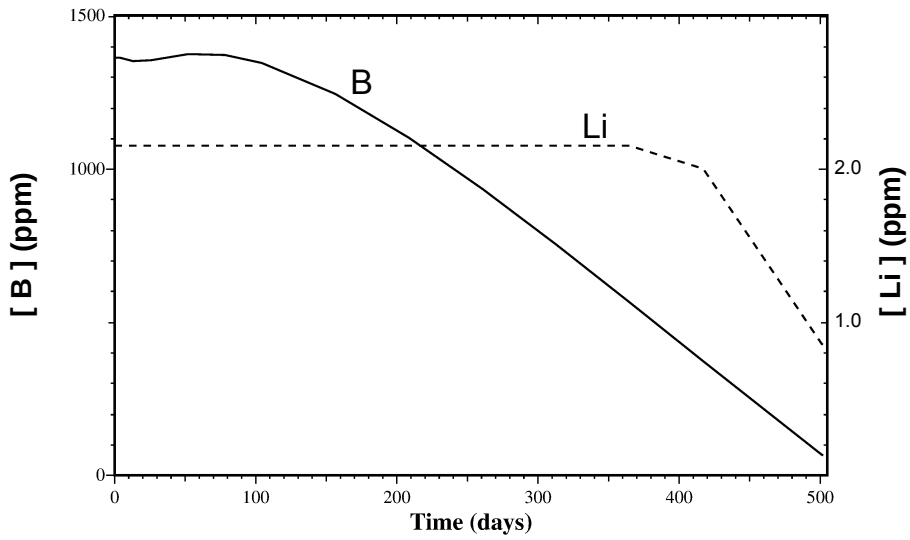

Figure 3: Boron and Lithium letdown curves (Seabrook cycle 5).

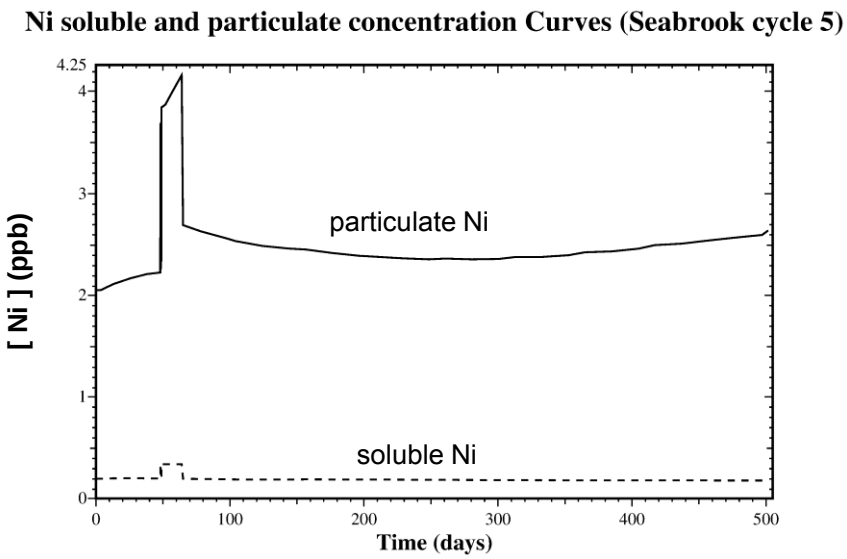

Figure 4: Nickel soluble and particulate concentration curves (Seabrook cycle 5).

Table 1 – Seabrook PWR main parameters.

Parameter	Value
Core Power (MW_{th})	3411
Inlet Temperature (Deg F)	558.8
Total Flow (gpm)	400800
Bypass Fraction (%)	5.8
Pressure (psia)	2250

2 TEST PROBLEMS AND SENSITIVITY STUDIES

2.1 Description of sensitivity studies

A series of sensitivity studies have been carried out in order to investigate the effects of the coupling scheme time stepping and selected physical parameters on the amount and patterns of CRUD deposits on PWR fuel rods.

The sensitivity studies have been performed using a single pin cell or a 5x5 sub-assembly as test problems. Details on the geometry and boundary conditions are given in chapters 2.2 and 2.3.

Studies with the 5x5 sub-assembly model:

1a) STAR-CCM+/MAMBA simulation for a depletion cycle of a Seabrook 5x5 sub-assembly, employing pin power profiles calculated by means of the Westinghouse multi-dimensional nodal code ANC [1];

2a) STAR-CCM+/MAMBA simulation for a depletion cycle of a Seabrook 5x5 sub-assembly, employing pin power profiles (including azimuthal power distributions) calculated by means of the neutron transport code DeCART [3].

It has to be noted that in these two studies the change in power distribution along the depletion cycle is computed without taking into account any feedback from the STAR-CCM+/MAMBA results.

Studies with the single pin cell model:

1b) Time stepping study running STAR-CCM+/MAMBA with fixed time steps

2b) Influence of Turbulence model

Studies on the effect of fixed-point Gauss-Seidel iteration, wall roughness and grid interpolation when mapping non-conformal meshes will be performed in the future.

2.2 Problem Description – Seabrook 5x5 fuel assembly

A 5x5 region of fuel assembly G70 was selected for the analyses presented here. The fuel assembly G70 contains two failed rods in locations G9 and L7, respectively (see Figure 5). The selected 5x5 region is highlighted in red, and contains one of the two failed rods (e.g. rod G9).

Eight grid spacers with mixing vanes are present on the fuel assembly. A three-dimensional (3D) perspective of the spacer design is presented in Figure 6. The geometry and dimensions of the spacer design and mixing vanes are reported in Figure 7 and Figure 8. The dimensions of fuel pins and guide tubes are given in Table 2. Since the exact geometry of the spacers could not be made available in time because of NDA issues, the geometry was based on the data published in Ref. [4]. The orientation of the mixing vanes was deduced from Ref. [5]. The axial location of the spacers was determined on the basis of the specifications of Vera benchmark problem #3 - 3D hot zero power (HZP) assembly [6]. The geometry specifications were summarized in a memorandum [7] and distributed within CASL for approval.

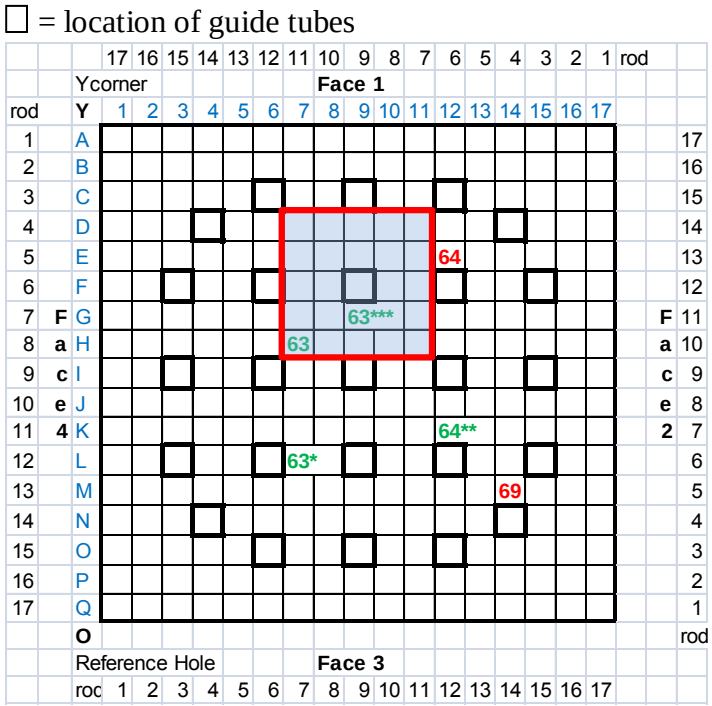

Figure 5: Seabrook Cycle 5 Assembly G70. The 5x5 region selected for STAR-CCM+/MAMBA simulations is highlighted by the red squared region.

Of all spacers present in the Seabrook Cycle 5 G70 fuel assembly, only the top three including mixing vanes have been modeled with STAR-CCM+ in order to limit the required computation time. In the future, a CFD model which includes all spacers will be adopted. The axial locations of the grid spacers modeled in the present simulations are shown in Figure 9. The axial region selected for the explicit CFD modeling of the grid spacers exhibits the highest pin powers and cladding temperatures. Therefore, it is expected that the thickest CRUD layers will be found in this region.

The report with the actual specifications of Seabrook cycle 5 fuel assemblies [2] was received on September 10th, at which time we realized a difference of several cm in the axial location of the spacer grids between the model used here and the Seabrook design (see chapter 6 for details). The width of the Seabrook spacer grids is also different than in our model. At the time the full specifications were received, we also realized that the orientations of the mixing vanes for spacer grid #6 are different than those for the other two spacer grids #5 and #7. The implication of this on the CRUD deposition patterns is discussed in detail in chapters 3.1 and 6.

The numbering convention adopted to identify individual fuel rods is shown in Figure 9 (right). With respect to the coordinate system centered in rod #01, illustrated in Figure 9, the azimuthal angle theta is defined as equal to 0° for (x =r; y = 0) where r is the radius of the rod, as 90° for (x =0; y = r), 180° for (x = -r; y = 0), and 270° for (x = 0; y = -r).

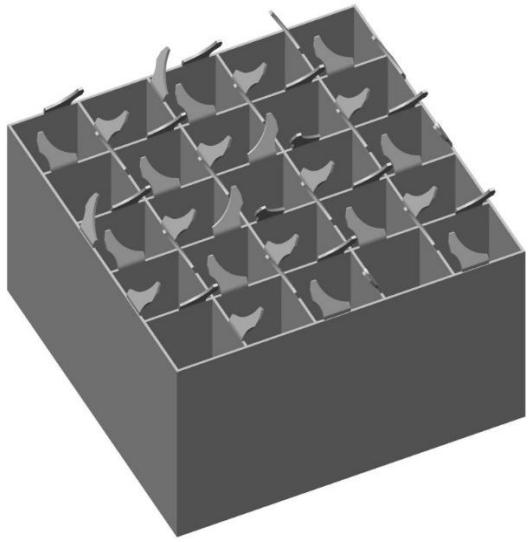

Figure 6: CAD for 5x5 grid spacer with mixing vanes.

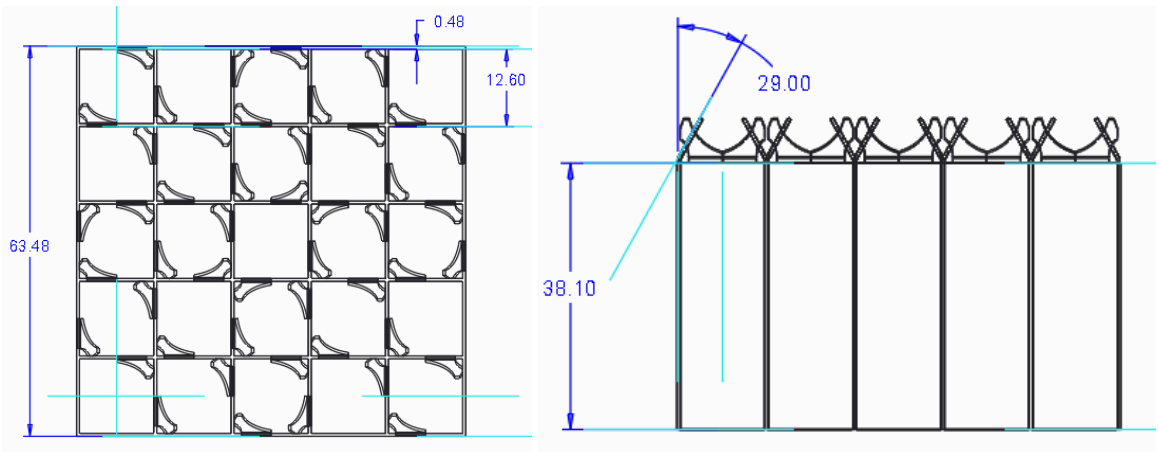

Figure 7: Spacers geometry and dimensions in mm.

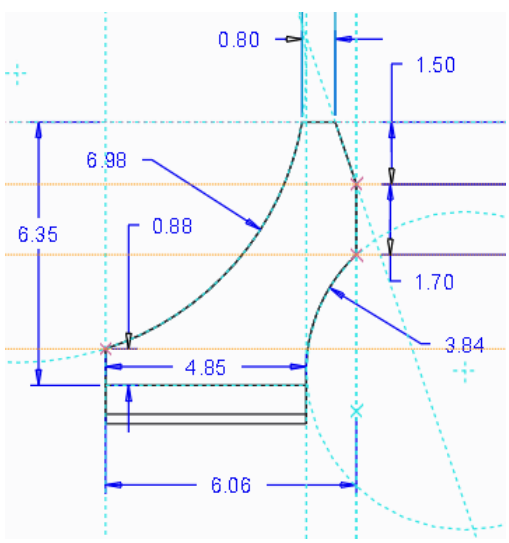

Figure 8: Geometry of mixing vanes with dimensions in mm.

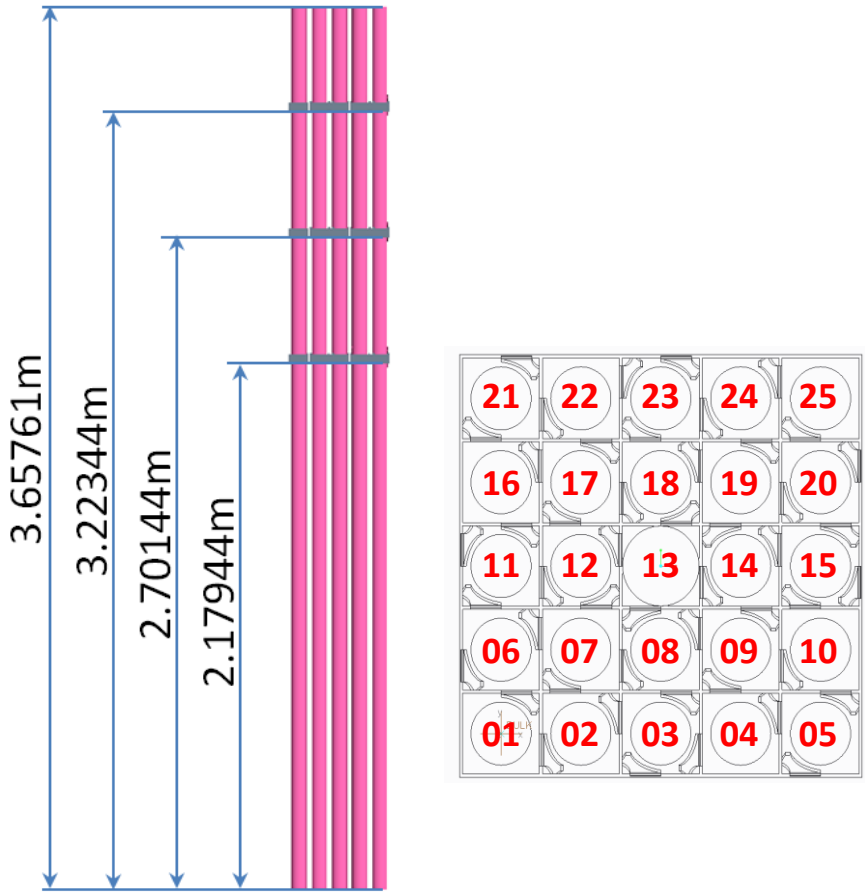

Figure 9: Axial location of grid spacers (left) and adopted rod numbering (right).

Table 2 – Dimensions of fuel pins and guide tubes.

Parameter	Value (cm)
Pin pitch	1.26
Fuel rod outer radius	0.4096
Fuel pellet outer radius	0.4666
Guide tube outer radius	0.602
Guide tube inner radius	0.561
Active fuel height	365.76

2.2.1 STAR-CCM+ model

The STAR-CCM+ computational mesh consists of over 64 M polyhedral cells. A mesh base size of 0.4 mm was adopted with 4 prism layers in the proximity of the wall. The fuel solid region is modeled as well to solve for the heat conduction within the fuel. The distribution of mesh elements among coolant, fuel, cladding and guide tubes is summarized in Table 3. A cross section of the mesh with zoom on a single pin is reported in Figure 10, while a detail of the mesh of the mixing vanes is reported in Figure 11.

An inlet velocity of 5.239 m/s and pressure boundary condition is imposed for the inlet and outlet axial planes of the coolant domain, respectively. Symmetric boundary conditions are

imposed on the lateral surfaces of the water domain. No-slip conditions are imposed on the grid spacers, pin walls and on the outer cladding surface. A volumetric power source is used in the fuel domain (provided by ANC or ANC/DeCART). The fluid-dynamic simulation includes conjugate heat transfer for the calculation of the temperature distribution in the fuel and cladding domains. The convergence criteria were fixed at 10^{-6} for continuity, momentum, and energy.

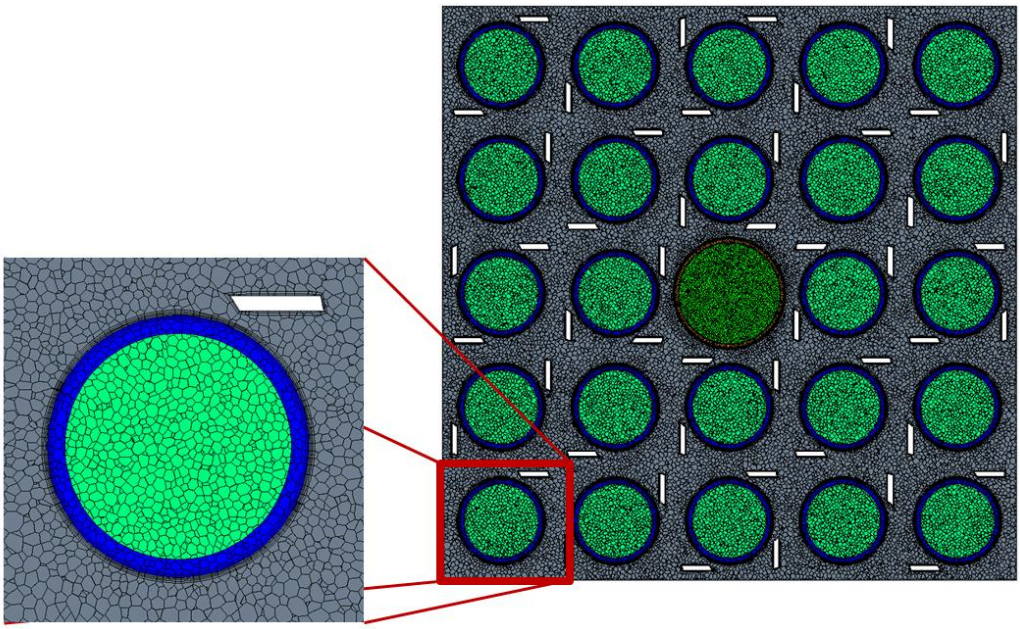

Figure 10: Cross-section of the CFD computational mesh.

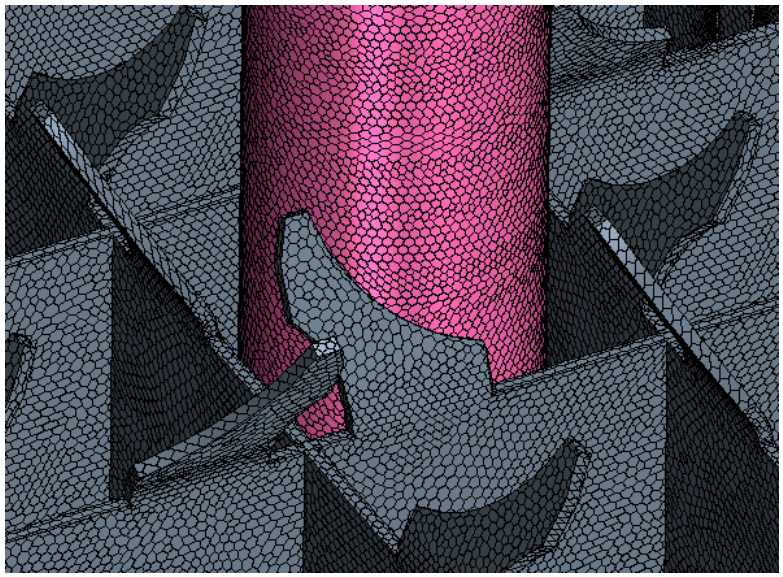

Figure 11: Detail of CFD computational mesh of mixing vanes.

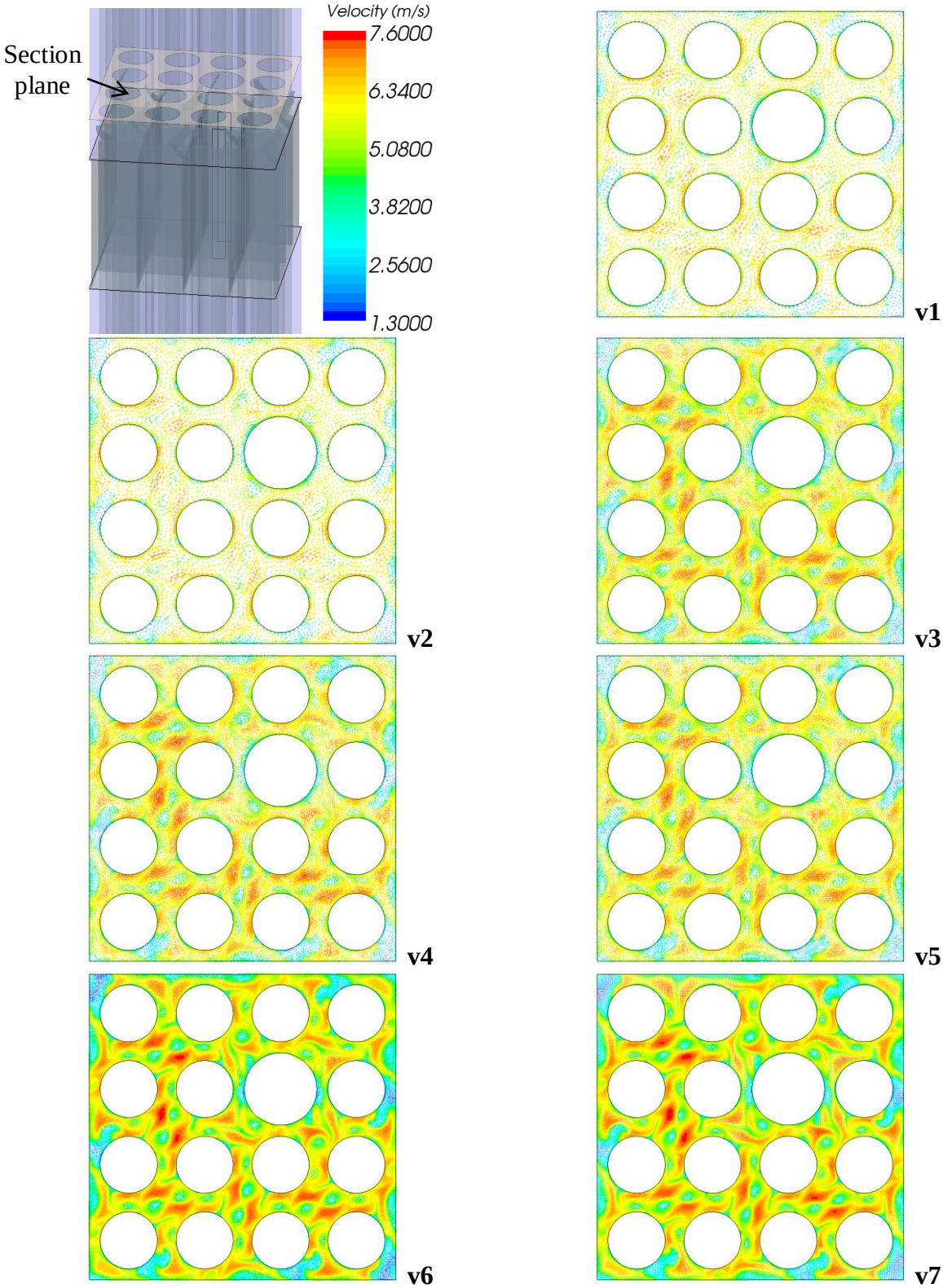

Figure 12: Magnitude of the velocity field above a grid spacer.

Table 3 –Summary of CFD mesh

	Fluid	Cladding	Fuel	GT
Cells	33,402,671	13,573,982	14,041,949	3,081,230
Faces	161,728,592	60,538,875	85,524,637	20,731,043
Vertices	112,379,469	45,224,451	70,251,624	17,608,914

Table 4 – Thermo-physical properties of materials.

Material	Property	Value
Fuel	Density [kg/m^3]	10400.0
	Specific Heat [J/kg-K]	300.0
Fuel Rod Cladding	Density [kg/m^3]	6500.0
	Specific Heat [J/kg-K]	350.0
	Thermal Conductivity [W/m-K]	17.0

Table 5 – Fluid properties and UO_2 thermal conductivity.

$\rho(T) = -1670.325859 - 4.84697*T + 0.01225*T^2 - 1.16905*10^{-5}*T^3, \quad \rho_{sat} = 594.17\frac{kg}{m^3}$	(1)
$\mu(T) = 3.111 + 0.03026*T - 0.8131*10^{-4}*T^2 + 0.4635*10^{-7}*T^3 + 1.677*10^{-9}*T^4 - 0.3094*10^{-12}*T^5 + 0.151*10^{-15}*T^6, \quad \mu_{sat} = 7.287*10^{-5}\frac{Pa}{s}$	(2)
$c_p(T) = \frac{T - 59160}{-167.5 + 4.091*10^{-4}*T^2} + 3659, \quad c_{p_{sat}} = 8513\frac{J}{kg*K}$	(3)
$k(T) = \frac{0.1183*10^{12} + 0.2419*10^{9}*T}{1 - 0.4177*10^{13}*T + 0.138*10^{11}*T^2}, \quad k_{sat} = 0.45833\frac{W}{m*K}$	(4)
$k_{UO2}(T) = 100*\left(\frac{1}{11.8 + 0.0238*T} + 8.775*10^{-13}*T^3\right)$	(5)

The thermo-physical properties of fuel and cladding materials are summarized in Table 4. All properties are assumed to be constant, with the exception of the UO_2 thermal conductivity which is assumed to be a function of the fuel local temperature. The adopted formulation is presented in Table 5, as are the coolant properties.

Within the limited time frame of the present milestone, it was not possible to conduct extensive mesh sensitivity studies. The criteria and parameters used to generate the mesh for the 5x5 model were based on previous sensitivities studies carried out on a 4x4 model of similar geometry. The 4x4 sensitivity studies were performed using six different polyhedral meshes of increasing refinement in which either the number of prism layers in the wall proximity or the base size of the computational mesh was varied (see Table 6 for more details on the mesh parameters). A seventh mesh (v7 in Table 6) was included in the study as well, characterized by the same parameters as the polyhedral finest mesh (v6), but employing trimmed elements instead of polyhedral. The different meshes were compared by analyzing the magnitude of the velocity field computed on a cross-section right above the mixing vanes of one of the grid spacers. The

results are reported in Figure 12. The location of the cross-section is shown on the top left corner of the figure. It can be observed that with a relative coarse mesh, characterized by a base mesh size of 0.4 mm (mesh v4), the velocity field can be reproduced with acceptable accuracy. Comparing mesh v6 with v7, it can also be concluded that with a given mesh base size and number of prism layers, trimmed meshes give results which are identical to the ones obtained with polyhedral meshes but require a slightly lower amount of computational cells to cover the same domain.

Table 6 – CFD mesh sensitivity study for rod bundle with grid spacer and vanes.

Case	Cells number* [M cell]	Base size, m	Number of prism layers	Mesh type
v1	1.9	6.0E-4	4	polyhedral
v2	2.5	5.0E-4	4	polyhedral
v3	5.0	3.5E-4	2	polyhedral
v4	5.6	4.0E-4	4	polyhedral
v5	6.7	3.5E-4	4	polyhedral
v6	25.4.	2.0E-4	4	polyhedral
v7	23.4	2.0E-4	4	Trimmed

(* - Cells number is given for fluid domain for single spacer)

2.2.2 MAMBA model

Figure 3 plots the boron and lithium coolant concentrations (in ppm) and Figure 4 plots the soluble and particulate Ni coolant concentrations (in ppb) as a function of time for Seabrook cycle 5. A short duration “spike” in Figure 4 is observed between approximately 45 and 65 days due to a temporary reduction in power (see Figure 2). A linear interpolation was applied to the curves in Figs. 3 and 4 to set MAMBA’s coolant concentrations of boron, lithium, soluble Ni, and particulate Ni at each time step. A constant average value of 32 cm^3/kg (STP) was used for the dissolved hydrogen concentration [8]. These concentrations are used by MAMBA’s internal thermodynamics models to compute the local pH and solubilities of various species of interest, such as: boric acid, lithium tetraborate, lithium monoborate, bonaccordite, nickel metal, nickel oxide and nickel ferrite. In this work, the solid skeleton of the CRUD layer was assumed to consist of only nickel ferrite (due to surface deposition of the particulates suspended in the coolant). The particulate surface deposition rate is governed by two temperature dependent Arrhenius rate coefficients: one for boiling and another for non-boiling regions. The boiling and non-boiling CRUD deposition rates were determined in previous studies [9, 10] and the same parameters were used unchanged in this work (see also Sect. 2.2.2). Depending upon the local internal CRUD temperature, the soluble Ni and boric acid species in the liquid within the pores of the CRUD can deposit and precipitate increasing the density of the CRUD layer especially near the cladding surface. Of the boron species, only the precipitation of lithium tetraborate was considered in this work (future studies will include the other boron species mentioned above). The pore fill rate due to the continual slow deposition of Ni within the pores of the CRUD was also determined in a previous study by comparing the MAMBA computed CRUD density with the experimental data from the WEC WALT loop [11].

MAMBA's 3D cylindrical grid consisted of 148 axial nodes with a uniform spacing of dz = 2.5cm. The bottom boundary node was located at z(0) = -2.5cm so that z(1) = 0 (the bottom of the rod). The top boundary node was located at z(148) = 367.5cm so that z(147) = 365cm (the top of the active part of the rod to be simulated). Zero heat flux boundary conditions were used at both ends of the rod to set the temperature values at z(0) and z(148). The azimuthal grid consisted of 16 azimuthal nodes with a uniform spacing of $d\theta = 22.5°$ with $\theta(0) = 11.25°$ and $\theta(15) = 348.75°$. The radial grid is an adaptive time dependent grid which varies as a function of the local CRUD thickness. A uniform radial spacing of dr = 5 µm was used with r(0) = 0 corresponding to the cladding surface. A thin "seed" layer (5µm) of CRUD was initialized along the entire 2D surface of the rod at time zero. The STAR-CCM+ computed surface heat flux was used to set the MAMBA temperature boundary condition at r(0) and the STAR-CCM+ computed CRUD/coolant surface temperature was used to set the MAMBA CRUD/coolant temperature boundary condition. The 3D temperature distribution within the CRUD layer was computed by iteratively solving a general 3D non-linear heat transport equation with internal "sinks" due to chimney boiling. The effective bulk CRUD thermal conductivity is a function of the local CRUD properties such as temperature and porosity (ε) and is computed using a mixing fraction: $k_{eff} = (1 - \varepsilon)k_s + \varepsilon\, k_w$ where k_s and $k_w(T)$ are the thermal conductivities of solid CRUD and water, respectively. A similar expression is used to compute the CRUD's effective bulk specific heat capacity. The chimney boiling model is a modified Cohen type model where the bulk heat power density (W/cm^3) leaving a given CRUD volume element is expressed as $q = Hc\, N_c\, A_c\, \kappa\, (T - T_{sat})$ where H_c is an effective bulk chimney heat transfer coefficient, N_c is the chimney surface density, A_c is an effective bulk chimney boiling surface area (which is a function of the chimney radius), κ is a porosity dependent CRUD permeability, T is the local CRUD temperature, and T_{sat} is the local liquid saturation temperature (which is a function of the local soluble boric acid concentration). The chimney parameters and the CRUD thermal conductivity k_s were previously optimized by fitting the MAMBA computed CRUD temperature to the experimental WEC WALT loop data [11]. These values are discussed in a previous report [9, 10] and were unchanged in this work (see also Sect. 2.3.2). We note that if $T < T_{sat}$ then q is set equal to zero (i.e., there is no internal chimney boiling in that CRUD volume element). The boiling heat flux q given above acts as a localized "sink" in the heat transport calculation and it is also used to compute the radial flow velocity of the coolant into the CRUD layer. The radial flow replenishes and concentrates the various soluble species within the pores of the CRUD (i.e., boric acid and Ni). The concentrations of these species can increase significantly near the cladding surface if the advective flux of the soluble species due to boiling induced flow is significantly greater than the concentration gradient induced diffusive flux in the opposite direction. Both the radial flow and diffusion are included in MAMBA's internal mass transport calculations. These mechanisms contribute to the precipitation of the boron species within the pores of the CRUD and also to the densification of the CRUD near the cladding surface (due to the slow Ni deposition inside the pores).

The thermal resistance and thickness of the CRUD layer are computed by MAMBA and written to a file for input by STAR-CCM+ at each depletion step. The thermal resistance R_{th} (°C m^2/W) is computed from the expression $R_{th} = \Delta T/Q$ where ΔT is the temperature drop (°C) across the CRUD layer and Q is the total heat flux (W/m^2) through the CRUD layer. We note that in boiling regions the heat removed due to boiling (the q discussed in the preceding paragraph) reduces the temperature drop across the CRUD layer. The smaller ΔT results in a smaller effective thermal resistance. The thermal resistance and CRUD thickness is used by STAR-CCM+ to update its

internal conjugate heat transfer calculation (which accounts for the temperature drop across the CRUD layer, see Section 3.1.1 below).

2.2.3 Power distribution from ANC – no azimuthal variation (case 1a)

The pin by pin power distribution was computed by Westinghouse using the ANC 3D nodal code. This code is based on the neutron diffusion approximation and utilizes the pin power reconstruction method to compute pin power distributions. However, ANC does not provide azimuthal (or radial) power variations within the pin.

The 3D power distributions were computed at 13 burnup states; Table 7 summarizes the burnup states in MWd/MTU and EFPD as well as the assembly relative power and coolant boron concentration. Figure 13 shows the radially-averaged axial power distribution for select burnup states.

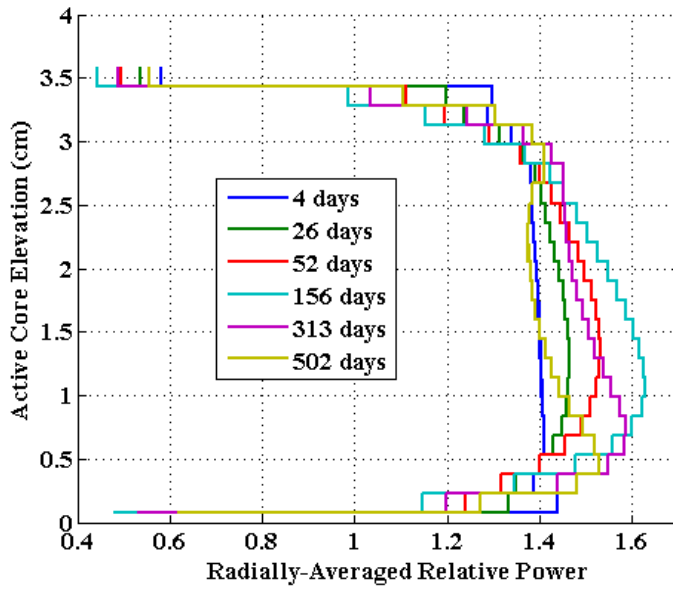

Figure 13: Axial power distribution of G70 assembly at select burnup states.

Table 7 – ANC burnup steps and relative power of G70 assembly.

Burnup Step	Effective Full-Power Days (EFPD)	Burnup (MWd/MTU)	Relative Power	Coolant Boron (ppm)
1	4	150	1.320	1362
2	13	500	1.322	1351
3	26	1000	1.329	1354
4	52	2000	1.344	1374
5	78	3000	1.357	1372
6	104	4000	1.366	1345
7	156	6000	1.377	1244
8	209	8000	1.380	1101
9	261	10000	1.377	934
10	313	12000	1.370	753
11	365	14000	1.361	564
12	417	16000	1.349	372
13	502	19242	1.330	65

2.2.4 Power distribution from DeCART with azimuthal variation (case 2a)

The ANC pin power distributions were adjusted to include azimuthal variation (circumferentially around the rod). The normalized azimuthal variation of the power was computed using DeCART. A 5x5 pin cell model including the guide thimble and IFBA-coated pins was constructed. The sub-assembly was depleted according to the same burnup states shown in Table 7. The sub-pin level power distribution computed by DeCART includes radial, azimuthal, and axial dependence. The axial discretization was the same as in the ANC model, and the radial and azimuthal discretization for a representative plane is shown in Figure 14. The azimuthal variation of the power is clearly demonstrated in the pins surrounding the guide thimble. Five equal volume radial regions exist within each fuel cell and 16 azimuthal regions are defined in each pin cell. To extract the azimuthal power distribution for a given plane within a given pin, the radial regions belonging to each azimuthal region were averaged. Then, the 16 azimuthal power values were normalized, and the ANC power distributions were adjusted, while ensuring the total power was persevered in each planar segment for all pins.

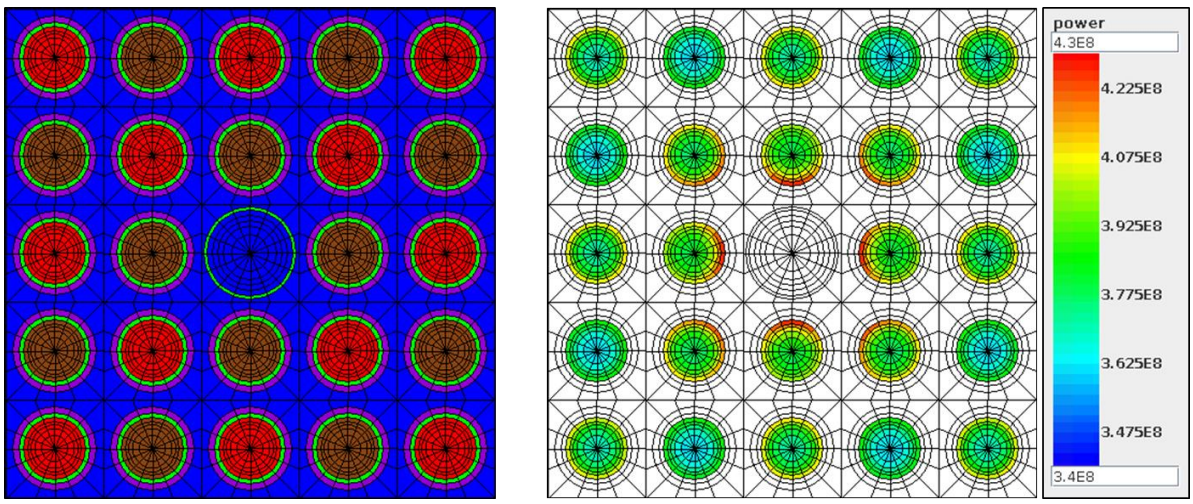

Figure 14: DeCART 5x5 model showing material regions (left), and radial and azimuthal power distribution for mid-plane at 4 days (right).

The normalized variation in the azimuthal power for the four pins surrounding the guide tube is shown in Figure 15. Variations in the azimuthal power approach 3% for the side of the pins that face the guide tube. This increase in power occurs due to the additional water present within the guide tube, which increases neutron moderation (slowing), and subsequently results in additional fissions. The uranium-235 low energy neutron fission cross section is higher than for high energy neutrons. Figure 16 compares three distinct pin locations: pin 1 far from the guide tube, pin 9 diagonal to the guide tube, and pin 8 directly next to the guide tube. Power variations approach 1.5% for pins diagonal to the guide tube and less than 0.5% for pins far from the guide tube.

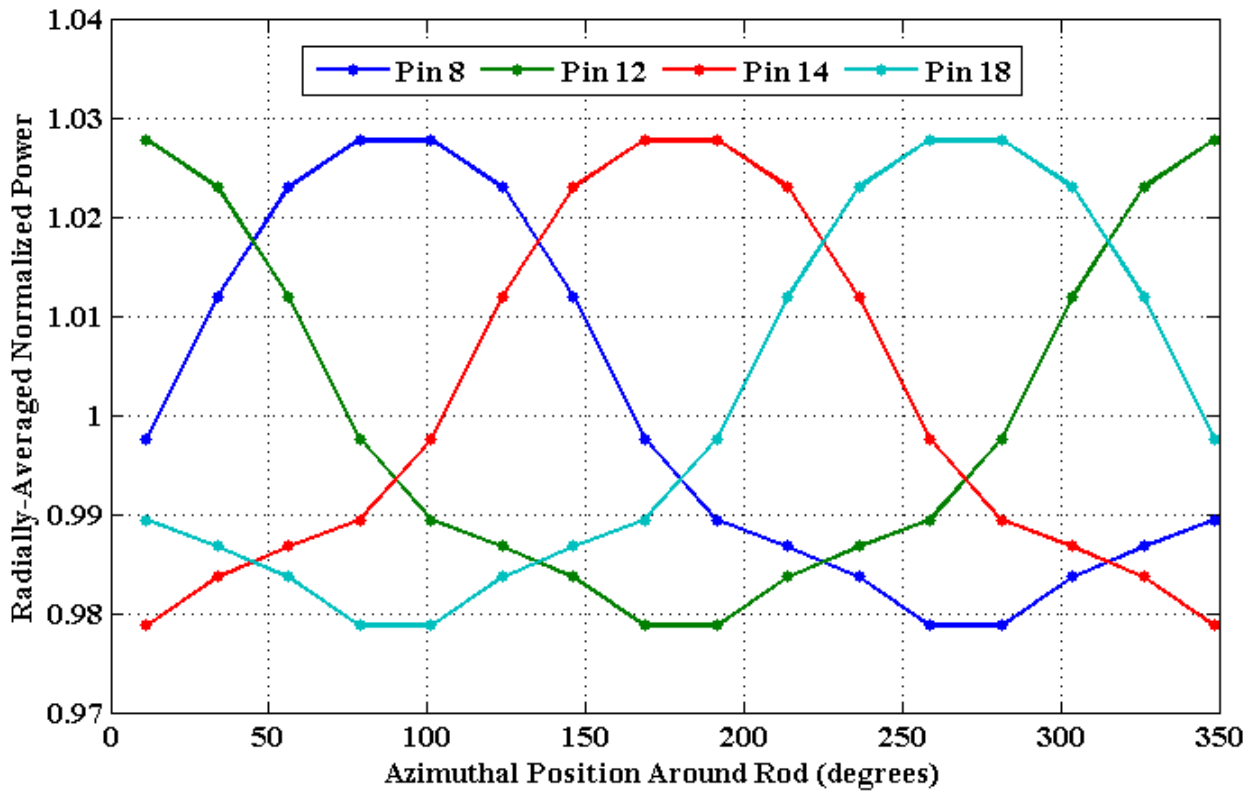

Figure 15: Azimuthal power variation for pins surrounding guide tube, plane 12, 4 days.

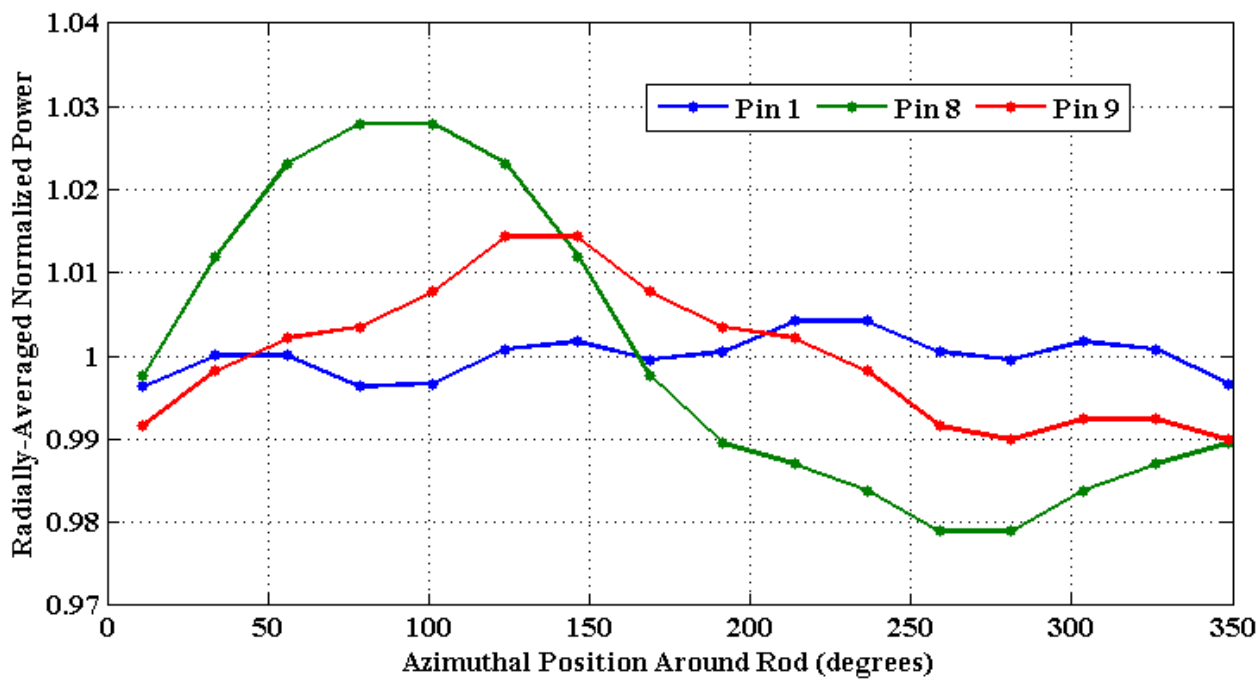

Figure 16: Azimuthal power variation for pins 1, 8, and 9, plane 12, 4 days.

2.3 Problem Description – Single Pin

For the single-pin test problem the same geometry already used for the 2011 MPO L1 report [12] was employed. As shown in Figure 17, three grid spacers were modeled in the upper regions of the pin.

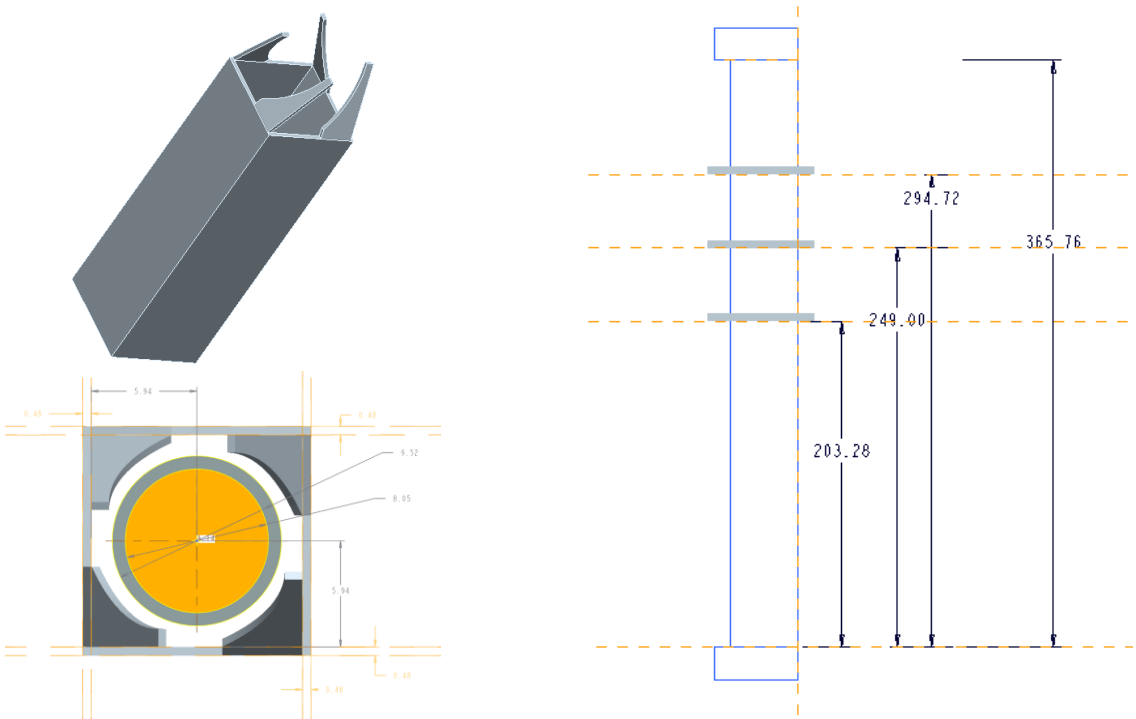

Figure 17: Pin cell model.

The model parameters are as follows:

Pin radius	0.4025 cm
Clad radius	0.4759 cm
Active fuel height	365.76 cm
Pin Enrichment	4.9 w/o
Inlet velocity	5.278 m/s
Inlet Temperature	556.76K
Pressure	15.51 MPa

2.3.1 STAR-CCM+ model

The CFD domain includes the solid structure containing the fuel pellet and cladding, the water domain in the subchannel surrounding the fuel pin, and the grid spacers. An inlet velocity of 5.278 m/s, an inlet temperature of 283.61ºC, and a pressure boundary condition is imposed for the inlet and outlet axial planes of the coolant domain, respectively. Symmetric boundary conditions are imposed on the lateral surfaces of the water domain. No-slip conditions are imposed on the grid spacers, pin walls and on the cladding surface. A volumetric power source is used in the fuel domain (provided by DeCART). The coolant density was calculated according to the following third-order polynomial:

$$\rho(T) = -0.0000116905\,T^3 + 0.01225\,T^2 - 4.84697\,T + 1670.3259$$

The inlet temperature is 556.76 K, and the system pressure is 15.51 MPa. The UO_2 fuel and cladding thermal conductivity are set constant at 3 and 17 W/m-K, respectively. The fluid-dynamic simulation includes conjugate heat transfer for the calculation of the temperature distribution in the fuel and cladding domains.

The CFD domain was meshed by means of polyhedral cells. Three explicit grid spacers including four mixing vanes, as shown in Figure 18 (left) are modeled. The five other spacers were not modeled to reduce computation time. The grid spacer regions, which rest at 203.28 cm, 249.00 cm, and 294.72 cm from the bottom of the active fuel, were discretized using polyhedral cells together with three layers of prismatic cells at the wall. The computational mesh upstream and downstream of grid spacers was generated by extrusion, applying the hyperbolic tangent law. Approximately 1.6 million cells makeup this model; additional mesh properties are summarized in Table 8. The convergence criteria were fixed at $1x10^{-6}$ for continuity, momentum, and energy. Figure 18 (right) shows the boundary conditions imposed and the cross section mesh.

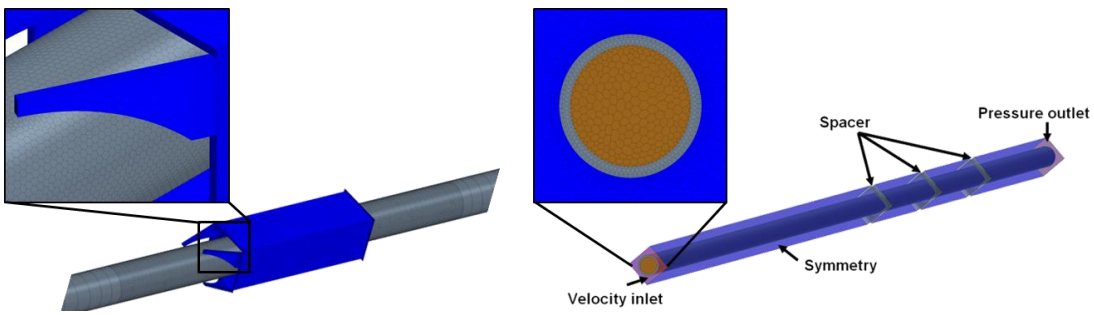

Figure 18: Grid spacer with mixing vanes (left) and boundary conditions and mesh (right).

Table 8 – STAR-CCM+ mesh information for single-pin model.

Region	Cells	Faces	Vertices
Fuel	430,803	2,642,496	2,214,928
Cladding	454,521	1,915,847	1,371,250
Fluid	776,970	3,401,427	2,283,715
Total	1,662,294	7,959,770	5,869,893

2.3.2 MAMBA model

The MAMBA model consists of the same fuel single pin cell geometry as previously discussed. The radial mesh of the CRUD region adapts to the CRUD growth in 5 µm increments, and the azimuthal mesh consists of 16 uniform regions. The pin is axially discretized into 148 uniform regions. The CRUD kinetics parameters are the same as used in the 5x5 simulation, described in Section 2.2.2. The coolant boron concentration is letdown according to Figure 3 and the values in Table 7.

3 TEST PROBLEMS AND SENSITIVITY STUDIES

3.1 RESULTS FOR SEABROOK 5x5 SUB-ASSEMBLY

3.1.1 STAR-CCM+/MAMBA simulation with ANC power distribution (case 1a)

The primary simulation consisted of a non-iterative, coupled MAMBA/STAR-CCM+ solution with an imposed 3D pin power distribution from ANC. Thirteen power distributions were extracted from Seabrook cycle 5 ANC simulation, according to the following time steps (days): 4, 13, 26, 52, 78, 104, 156, 209, 261, 313, 365, 417, and 502. The power distributions were updated in STAR-CCM+ throughout the depletion cycle. Figure 19 shows the time stepping algorithm; for each depletion step STAR-CCM+ performs a steady state thermal-hydraulic simulation followed by MAMBA's time-dependent CRUD deposition simulation. The coupling between MAMBA and STAR-CCM+ is two-way. As discussed above in Section 2.2.2, the MAMBA computed effective thermal resistance and CRUD thickness are passed back to STAR-CCM+ at each depletion step.

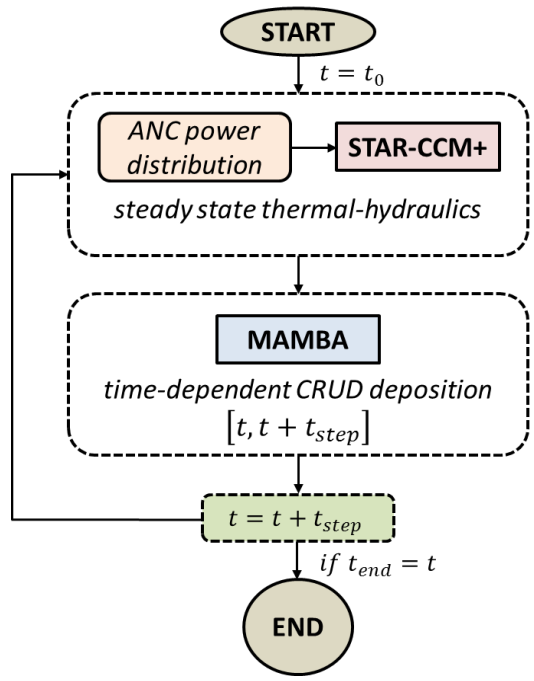

Figure 19: MAMBA/STAR-CCM+ time stepping algorithm for single pin cell time stepping study.

These quantities are used by STAR-CCM+ for updating its internal conjugate heat transfer calculation which includes the temperature drop across the CRUD layer. Likewise, the STAR-CCM+ computed rod surface heat flux and CRUD/coolant temperature are passed to MAMBA at each depletion step for updating the boundary conditions for MAMBA's internal 3D heat transfer calculation within the CRUD layer.

The computational times for the coupled 5x5 simulation for the full 502 day cycle were the following: The total MAMBA run time was approximately 5 hours per pin, so the total CPU time was 5*24 = 120 hours. The MAMBA calculations for the 24 pins were distributed across 6 cores (each pin calculation is independent from the others). The total STAR-CCM+ run time was approximately 194 hours on 62 cores for a total of 12,028 hours. Data processing of the MAMBA coupling files by STAR took about 15 hours on 62 cores for an additional 930 hours.

<u>STAR-CCM+ results (case 1a)</u>

The cladding temperature computed by STAR-CCM+ for days 4, 261 and 502 is reported in Figure 20 to Figure 22 respectively. The rows of pins are numbered following the convention depicted in Figure 9, so in Figure 20 pin #1 is the first on the left, and pin #25 is the last on the

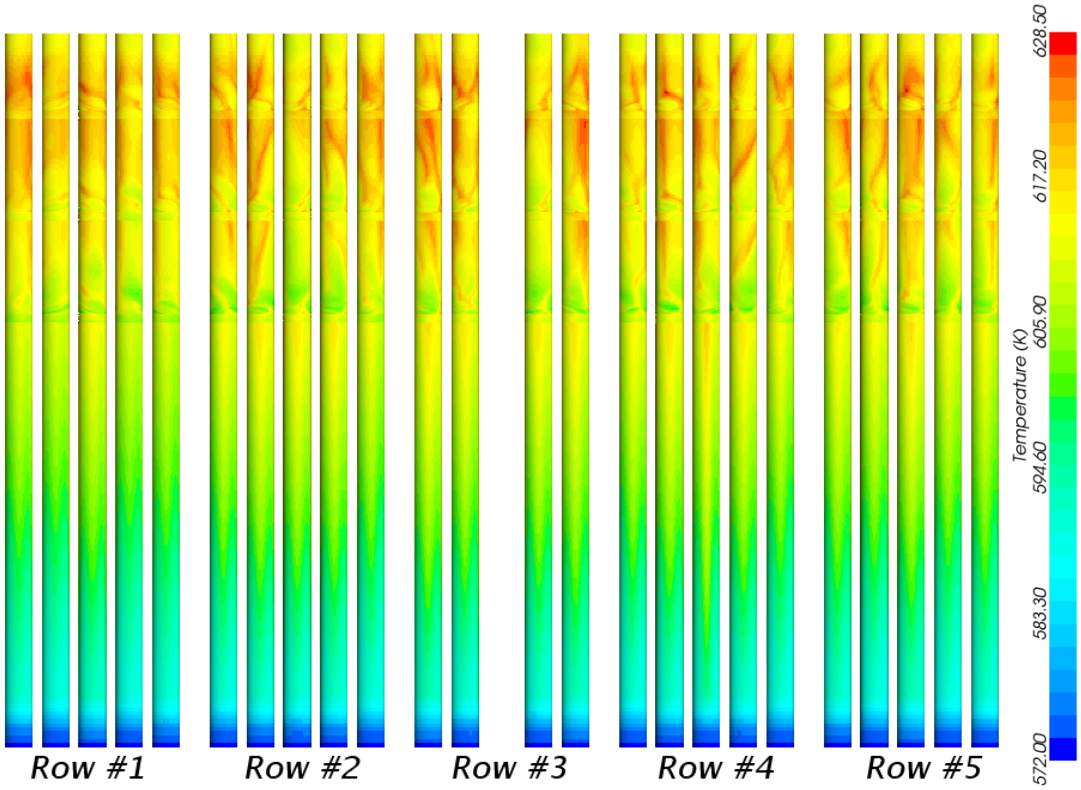

Figure 20: Cladding temperature at 4 days (case 1a).

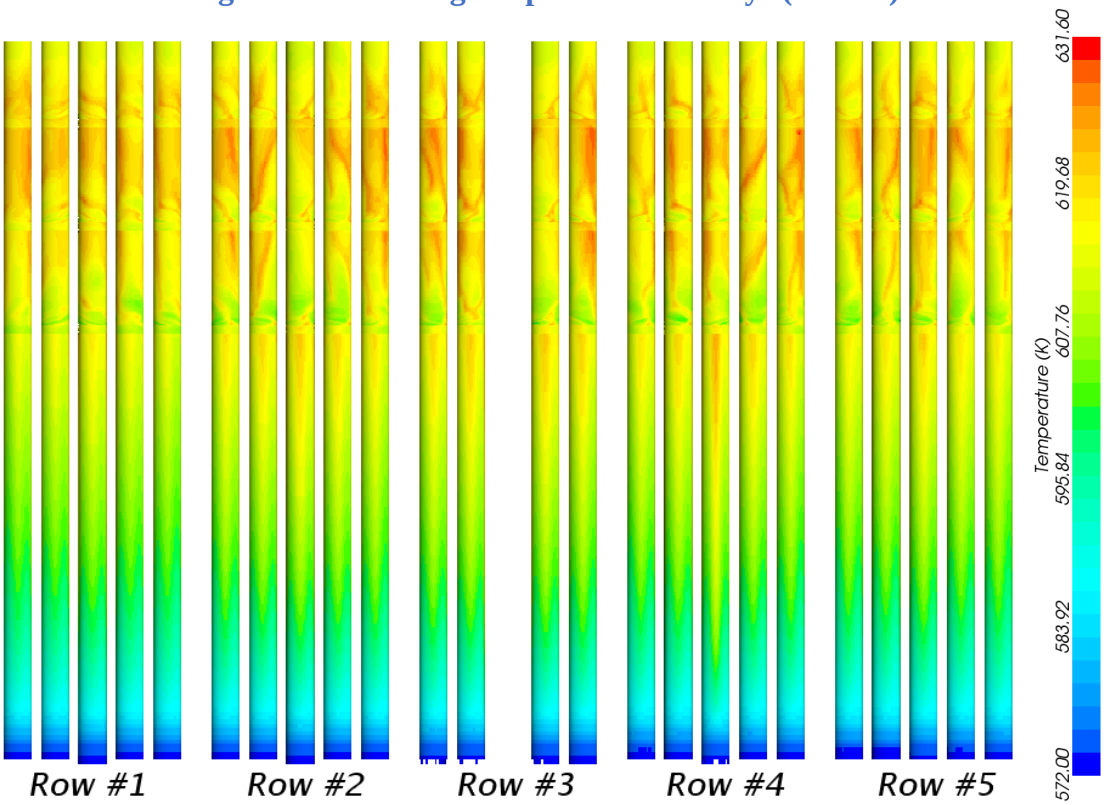

Figure 21: Cladding temperature at 261 days (case 1a).

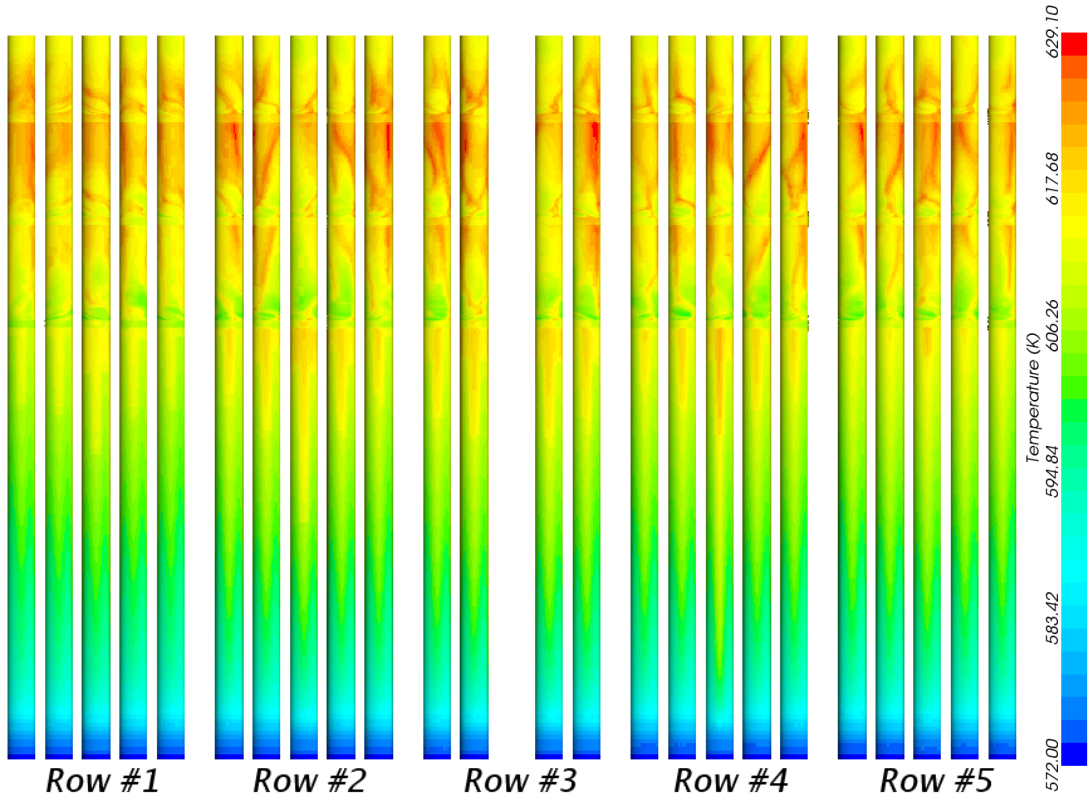

Figure 22: Cladding temperature at 502 days (case 1a).

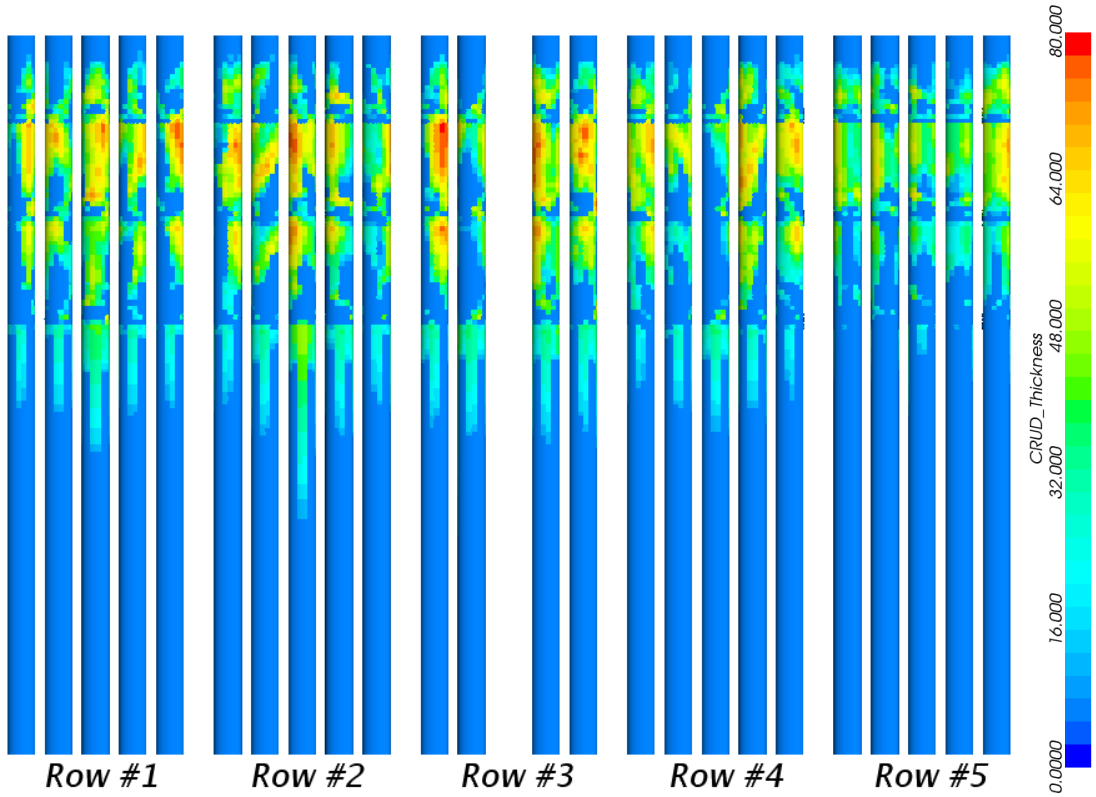

Figure 23: CRUD thickness [microns] at 502 days (case 1a).

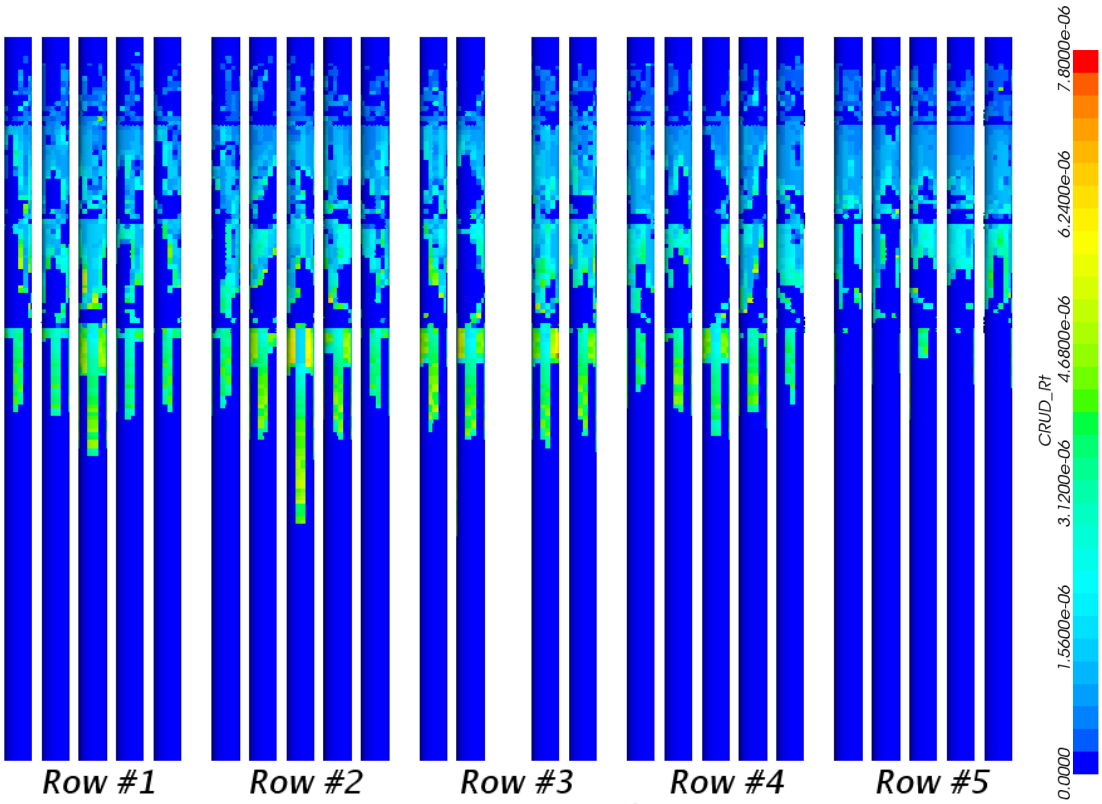

Figure 24: CRUD thermal resistance [m^2K/W] at 502 days (case 1a).

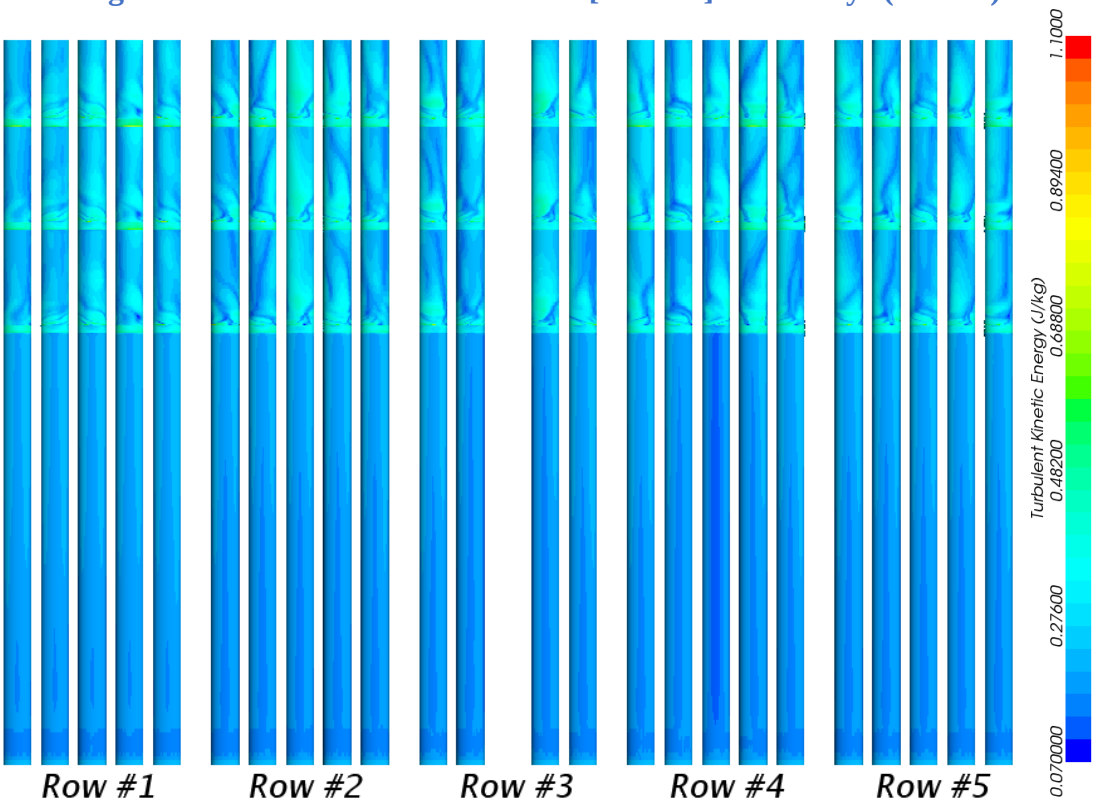

Figure 25: Turbulent kinetic energy at 502 days (case 1a).

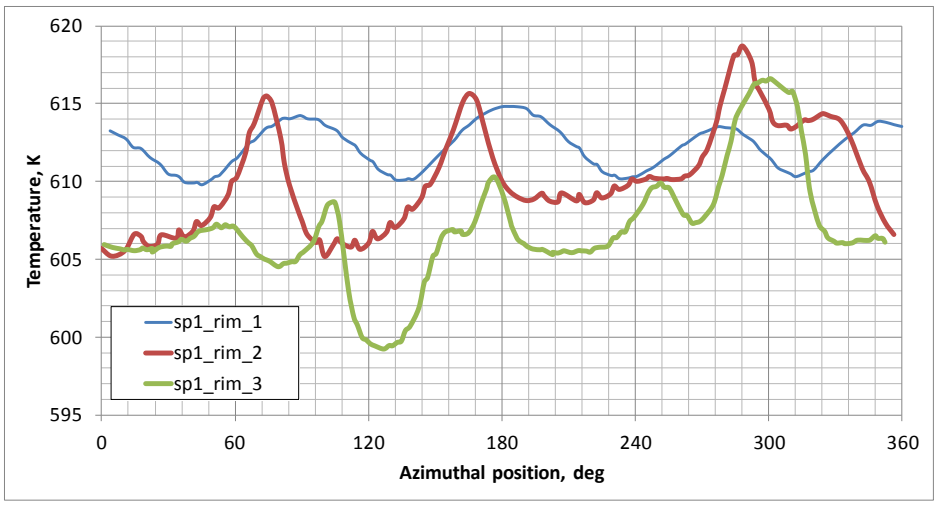

Figure 26: Azimuthal distribution of cladding temperature for pin #8, spacer 1, at 4 days.

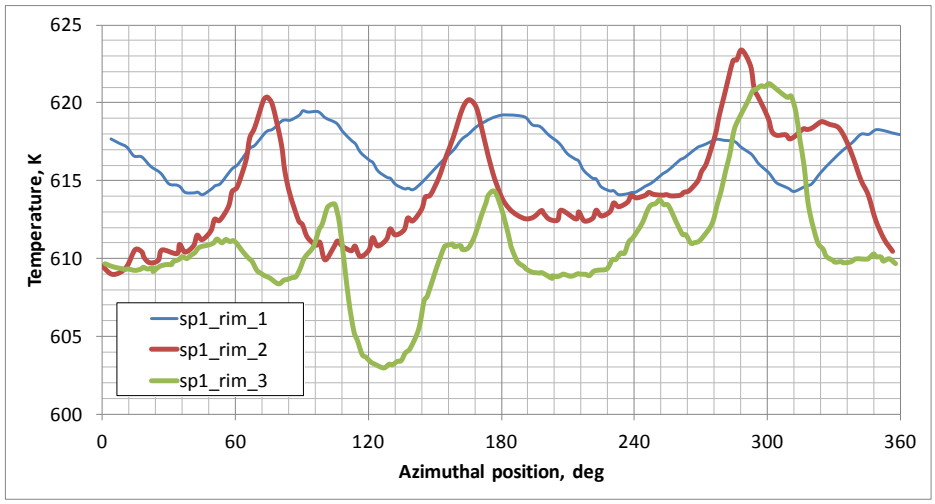

Figure 27: Azimuthal distribution of cladding temperature for pin #8, spacer1, at 261 days.

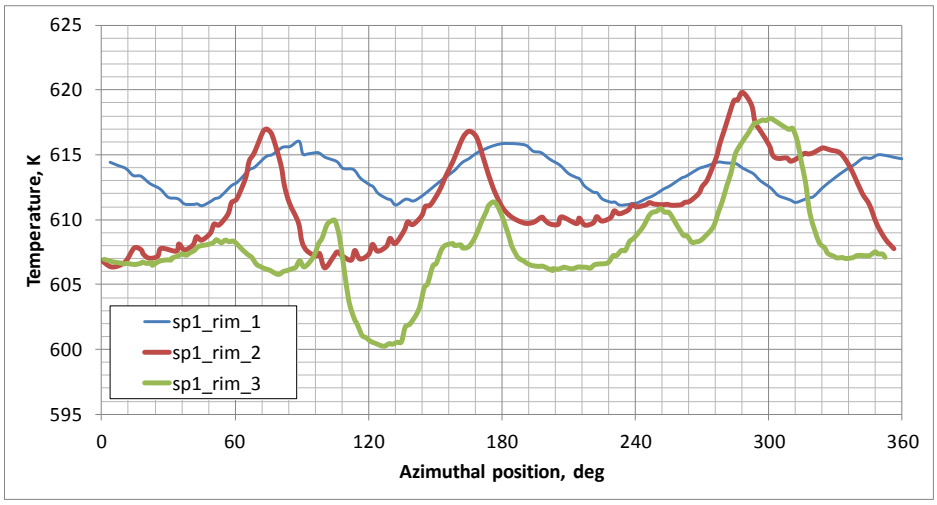

Figure 28: Azimuthal distribution of cladding temperature for pin #8, spacer1, at 502 days.

right. The middle pin in row #3 is occupied by the water rod, and therefore it is not shown. Same conventions are used for the successive figures. The evolution of the cladding temperature from

day 4 to day 502 in Figure 20 to Figure 22 is a result of the change in power along the cycle and the growing thermal resistance induced by the deposition of CRUD on the fuel rods.

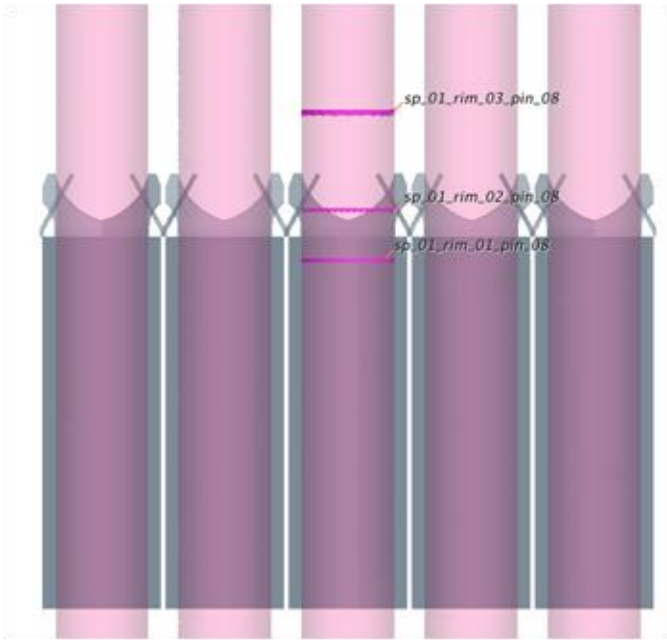

Figure 29: Axial location along grid spacer for azimuthal distributions of Figure 26 to Figure 28.

The azimuthal temperature distributions for pin #8 at three different elevations in the proximity of spacer #1 of the modeled spacers (see Figure 9 for exact axial location) are reported in Figure 26 to Figure 28 for days 4, 261, and 502 respectively. The locations of the three elevations are illustrated in Figure 29, with rim 1 being upstream and rim 3 downstream of the mixing vanes. Upstream of the mixing vanes, the azimuthal variations of the cladding temperature are due by the different amount of coolant that is surrounding the pin surface in view of the subchannel geometry. Downstream of the mixing vanes, the temperature azimuthal variations are amplified by the flow swirl that the vanes induce. The flow swirl causes also a phase shift in the azimuthal temperature distribution.

The temperature distributions obtained for days 4 and 261 (Figure 26 and Figure 27 respectively) are modulated by the change in power during the cycle, but the effect of the CRUD induced thermal resistance is still not visible. The effects of the CRUD build-up on the cladding temperature becomes apparent when the comparison is extended to later times in the cycle (see distribution at 502 days in Figure 28).

At 502 days, a considerable amount of CRUD has deposited on the rod surface, as shown in Figure 23. The corresponding thermal resistance added by the CRUD on the rod surface can be seen in Figure 24. The patterns of the CRUD deposits in the simulation discussed here are solely caused by the flow swirls induced by the grid spacer mixing vanes, since no azimuthal power variation has been considered here. The flow swirl can be visualized by the turbulent kinetic energy in proximity of the rod surface (see Figure 25). As expected, this is strongly dependent on the orientation of the mixing vanes. The CRUD deposits are out-of-phase with the flow swirl (or with the turbulent kinetic energy) since regions of high turbulent kinetic energy correspond to higher heat transfer coefficients and higher CRUD erosion rates.

It is interesting to note that, because of the particular orientation of the mixing vanes, rod 8 exhibits high CRUD deposit thickness on the surface not facing the water rod. Additionally, the effect of the azimuthal variation of the power distribution induced by the presence of the water rod is discussed in chapter 3.1.2.

CRUD deposits upstream of spacer #1 tend to extend for a longer distance because the grid spacers at lower axial locations have not been included in the CFD model.

MAMBA results (case 1a)

The 5x5 subassembly and pin numbering are shown in Figure 30. The central 3x3 region of interest surrounding the guide tube is highlighted in red. As illustrated in Figure 19, the STAR-CCM+ solution at each depletion step was used to set MAMBA's heat transfer boundary conditions: the heat flux and CRUD/coolant temperature along the 2D surface of each rod. A separate MAMBA calculation was performed for each of the 24 rods keeping these boundary conditions fixed during the time intervals between the depletion steps. The STAR-CCM+ computed turbulent kinetic energy was also updated at each depletion step and used by MAMBA to set the CRUD's surface erosion rate. A simple surface erosion model is currently used in MAMBA for which the erosion rate is taken to be proportional to the STAR-CCM+ computed turbulent kinetic energy. The proportionality constant was identical to the value used in our previous studies [9, 10]. The same 3D cylindrical coordinate system was used internally by MAMBA for each pin (i.e., STAR-CCM+ shifted the origin of each pin before transferring its data to MAMBA). The bottom of the pin corresponds to z = 0 and the xy orientation was chosen such that the positive x axis points to the right and the azimuthal angle is zero degrees along the positive x axis (see Figure 30).

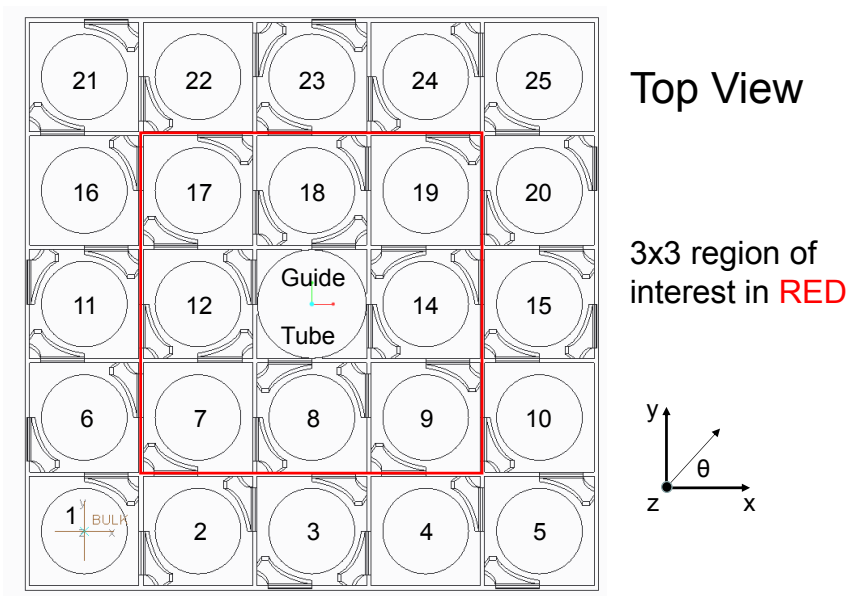

Figure 30: 5x5 pin designation with vanes orientation (same for grids 5, 6 & 7).

Three-dimensional perspective plots of the eight rods surrounding the guide tube are plotted in Figure 31 to Figure 33. A top down view of the 3x3 region is shown in Figure 31. The swirling CRUD patterns, mixing vane induced erosion effects, and 180° symmetry are clearly visible in the upper spans. The darkest red regions correspond to a CRUD thickness of 75 microns.

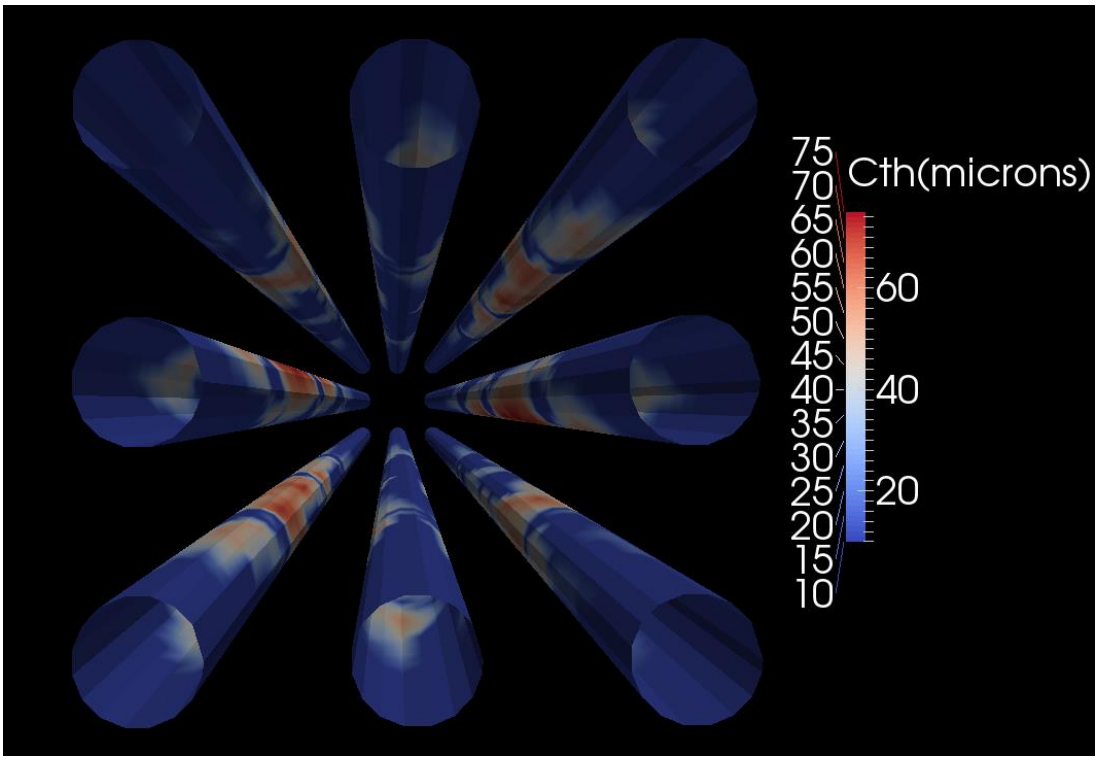

Figure 31: 3D top view of 3x3 surrounding the center guide tube at 502 days.

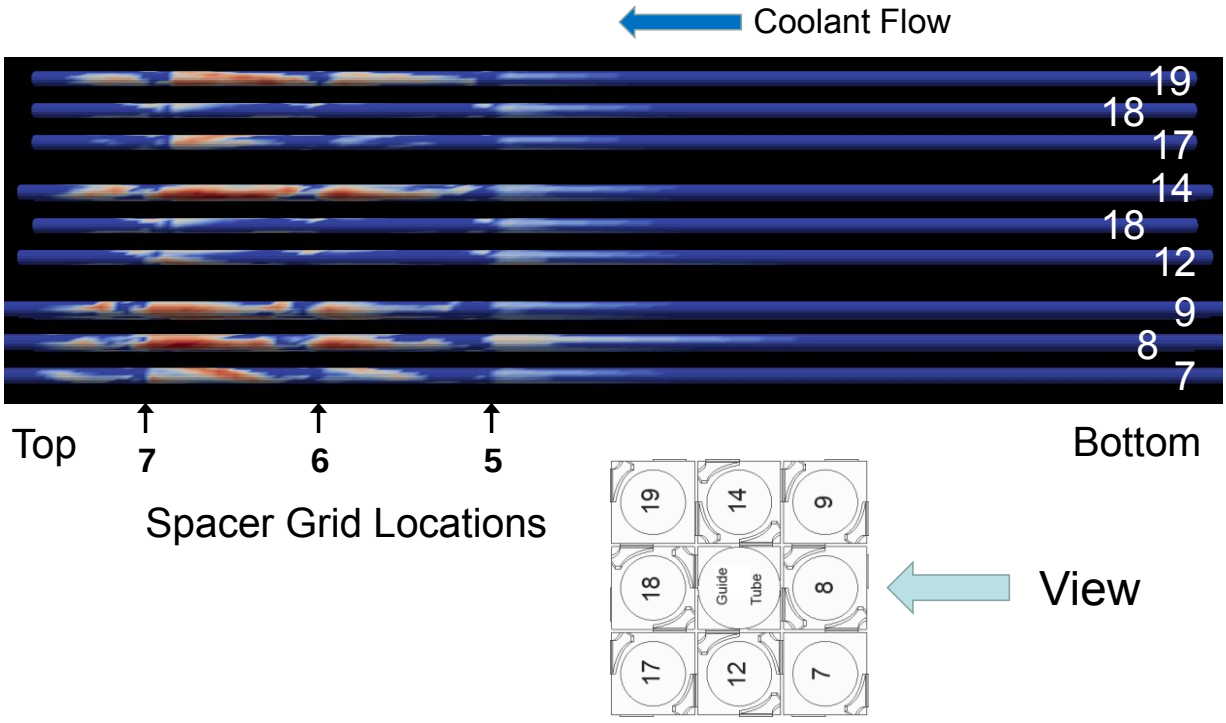

Figure 32: 3D face view of 3x3 at 502 days.

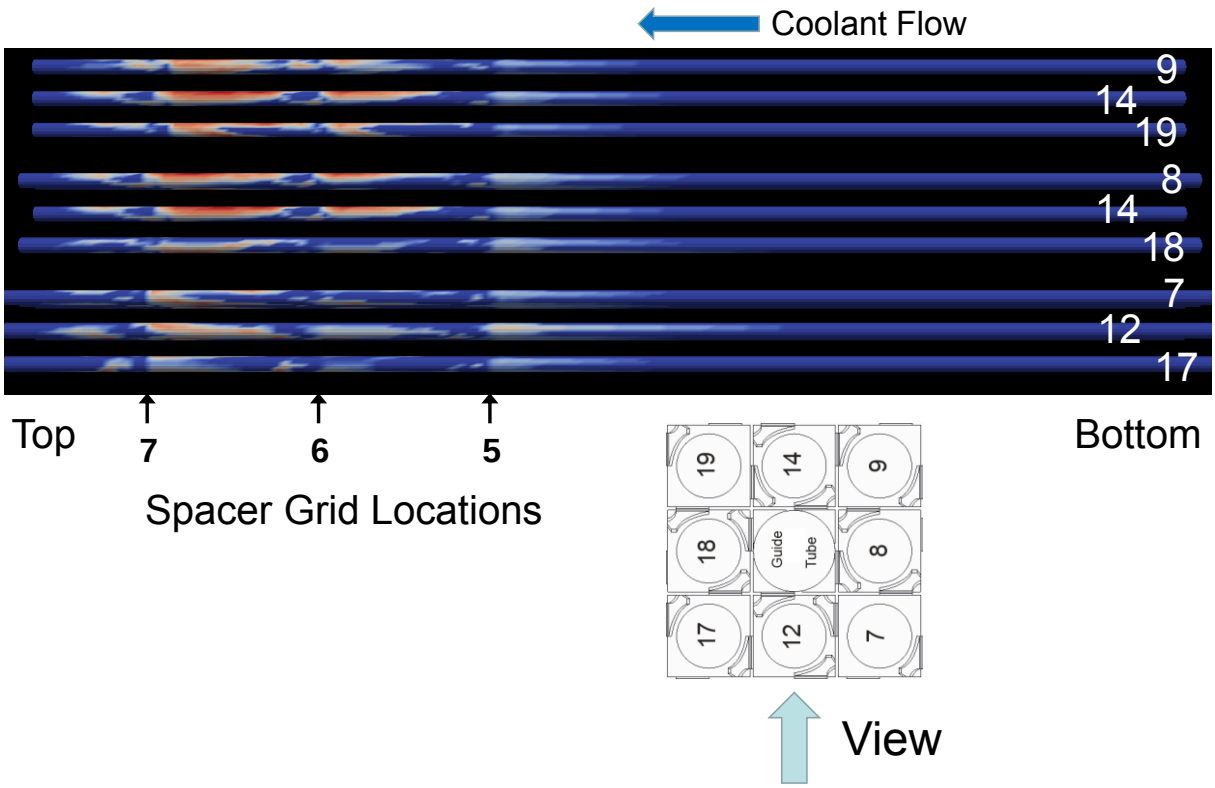

Figure 33: 3D face view of 3x3 at 502 days

Figure 32 shows a "front" face view looking at the 3x3 from in front of rods #7, 8 and 9. The top of the subassembly is on the left and the bottom on the right so that the coolant flow is from right to left. The locations of the spacer grids #5, 6, and 7 are labeled by arrows. Due to the 180° symmetry, the front face of rod #7 (bottom rod in Figure 32) is the same as the back face of rod #19 (top rod in Figure 32) and vice versa. Similar front/back symmetry holds for the other symmetric partners: (8, 18), (9, 17), and (12, 14). Figure 33 is similar to Figure 34 except that a "side" face view looking at the 3x3 from in front of rods #17, 12, and 7 is shown. As in Figure 32, front/back symmetry holds for the four symmetric partners mentioned above (i.e. the front face of rod #17 in Figure 33 is the same as the back face of rod #9 and vice versa).

Figure 35 plots the total CRUD mass on each rod integrated over the 3D MAMBA grid. The initial non-zero value of approximately 0.9g corresponds to the uniform 5 micron thick "seed" layer. A small jump in the mass accumulation rate is observed at 50 days due to the temporary spike in the Seabrook coolant Ni concentration (see Figure 4). The different colored curves correspond to the eight rods of the 3x3 surrounding the guide tube (see Figure 30) and the yellow curves correspond to the other rods of the 5x5 subassembly. Rods #12 (red) and 14 (blue) accumulate the most CRUD mass by the end of the cycle at 502 days. Figure 36 plots the maximum CRUD thickness on each rod as function of time. The same color scheme is used as in Figure 35. The maximum CRUD thickness at the end of the cycle varied between 70-80 microns. The CRUD thickness for rods #12 (red), 14 (blue), 8 (green), and 18 (brown) within the central 3x3 region around the guide tube reached a maximum of 75 microns. These CRUD thickness values are consistent with the Seabrook CRUD scrapes (see Sect. 6 for additional discussion).

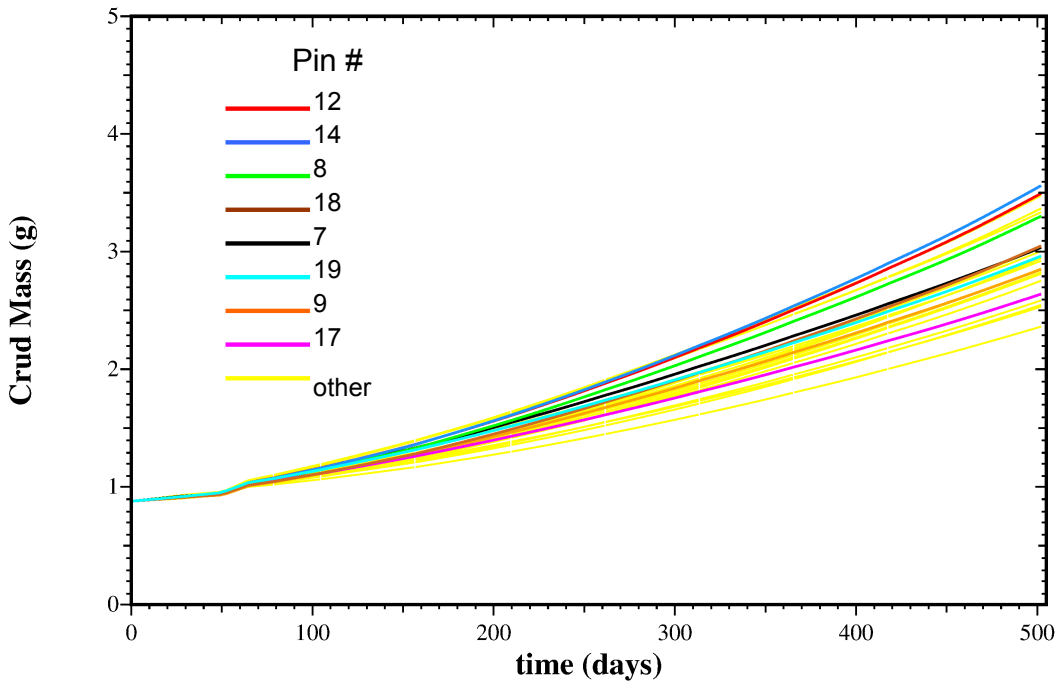

Figure 35: Total CRUD mass on each pin vs time

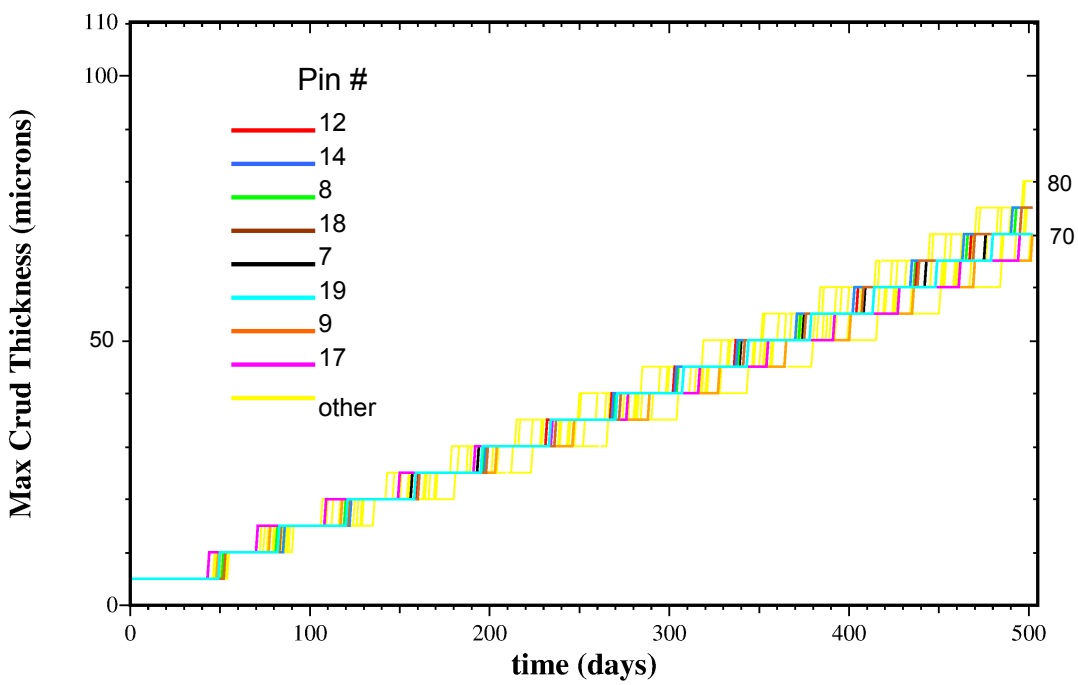

Figure 36: Maximum CRUD thickness on each pin vs time

Two-dimensional (2D) contour plots of the CRUD thickness at the end of Seabrook cycle 5 (502 days) are plotted in Figure 37 to Figure 39 as a function of azimuthal angle θ (deg) and axial height z (cm) for the eight rods surrounding the central guide tube (see Figure 30). The coolant flow direction is from the bottom (z = 0) to the top (z = 365cm) in these plots. The axial location of the top of the three spacer grids at 222, 274, and 326 cm are indicated by small arrows. Very

little CRUD (i.e, thickness < 10 microns) is deposited below grid #5 where the cladding surface temperature is lower and very little if any subcooled nucleate boiling (SNB) occurs (i.e. the cladding surface temperature is below the coolant's saturation temperature T_{sat}). Significant CRUD deposits occur above grid #5 with the largest amount of CRUD being deposited within span #6 (i.e., between grids #6 and 7). This trend is consistent with the Seabrook CRUD data (see Section 6 for a detailed comparison with the Seabrook data). The CRUD deposits track the coolant flow patterns and are thickest (yellow/orange colored regions) where the cladding surface is hottest and SNB occurs.

In contrast, very little CRUD deposits in the vicinity of the mixing vanes where the cladding surface temperature is lower and significant surface erosion occurs due to the large turbulent kinetic energy in these regions (i.e., the white CRUD free regions above grid #5). The open triangle and square in each plot mark regions of interest (thicker CRUD). The location of these features on the surface of each rod are designated by the corresponding solid triangle and square on the 3x3 pin map overlaid on each plot. The open/solid squares correspond to the thicker CRUD just below grid #5 which occurs on the hotter side opposite the side facing the guide tube for all eight pins of the 3x3. The open/solid triangles correspond to the thickest CRUD which consistently occurs in span 6 for all eight pins of the 3x3. As expected, the results are symmetric with respect to a 180° rotation about the center of the guide tube. That is, rods #12, 7, 8, 9 are 180° symmetric with rods #14, 19, 18, 17, respectively.

The dashed lines in Figure 37 for rod #8 and in Figure 38 for rod #12 show the location (or "slice") of the 2D CRUD profile plots for these two rods plotted in Figure 40 and Figure 41, respectively. The four 2D profile plots in Figure 40 for rod #8 and in Figure 41 for rod #12 show the CRUD's porosity, temperature, boiling heat flux, and boron concentration as a function of the axial height z (cm) and the radial distance from the cladding surface r (microns). By the end of Seabrook cycle 5, the density of the CRUD layer near the cladding surface has increased (i.e. the porosity has decreased from 0.7 (red) to 0.42 (yellow) which is consistent with the observations from Seabrook CRUD scrapes (see Section 6). The maximum CRUD thickness in span #6 for both of these pins is 75 microns and is also consistent with the Seabrook CRUD scrape data. The three "dips" in the CRUD's thickness at z = 222, 274, and 326 cm correspond to the location of the three spacer grids and are due to the reduced cladding surface temperature and surface erosion effects from the mixing vanes.

As expected, the CRUD temperature is hottest (red) in the denser regions near the cladding surface reaching a maximum temperature of approximately 348°C. The heat flux density due to chimney boiling within the CRUD layer acts as a local heat sink and also induces radial flow of liquid from the surface of the CRUD down into the CRUD layer. Significant boiling within the CRUD layer is indicated by the light-blue colored regions. The largest boiling (red) occurs near the surface of the CRUD. The boiling within the CRUD layer also enhances the CRUD's deposition rate leading to thicker CRUD in boiling regions (see Figure 42 to Figure 44). Soluble boric acid species concentrate near the cladding surface (red) due to the boiling induced flow. As the local boric acid concentration increases, it can eventually exceed the solubility limit for a solid phase boron compound such as lithium tetraborate ($Li_2B_4O_7$). Once the solubility limit is exceeded, the precipitation of the solid phase occurs which quickly fills a significant fraction of the pores while simultaneously shutting off the boiling induced flow in that region.

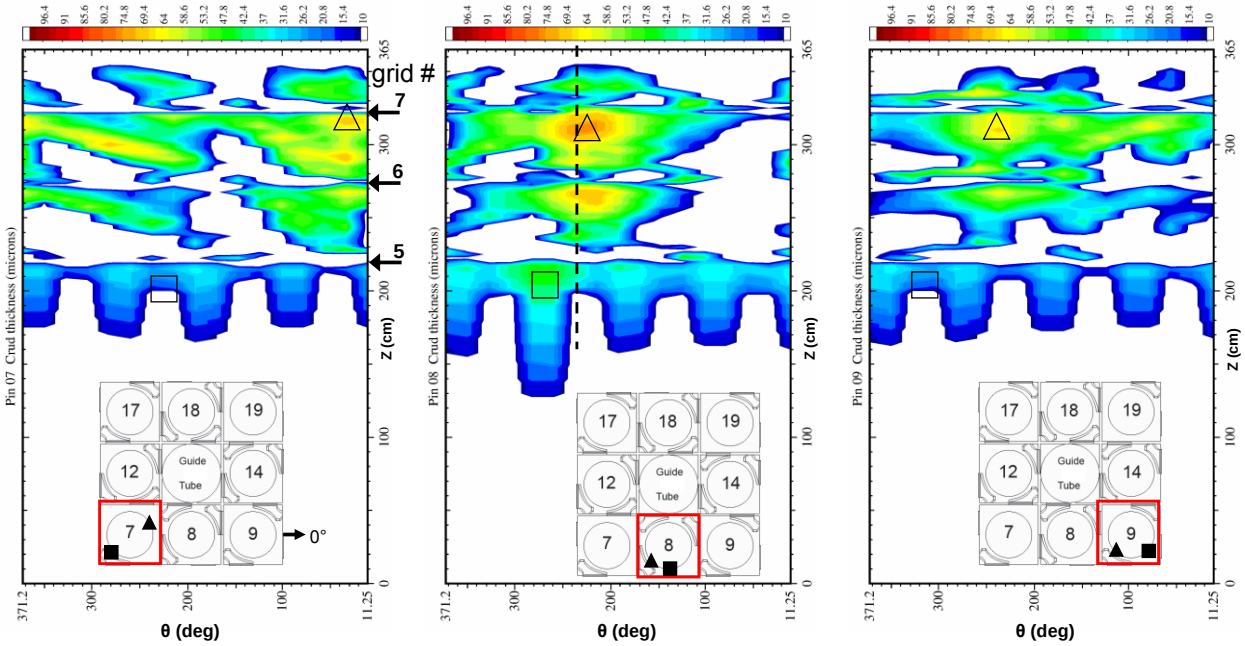

Figure 37: 2D surface contour maps of the CRUD thickness (in microns at 502 days) – pins 7 to 9. The dashed vertical line in the middle panel shows the location of the 2D profile plot in Figure 39.

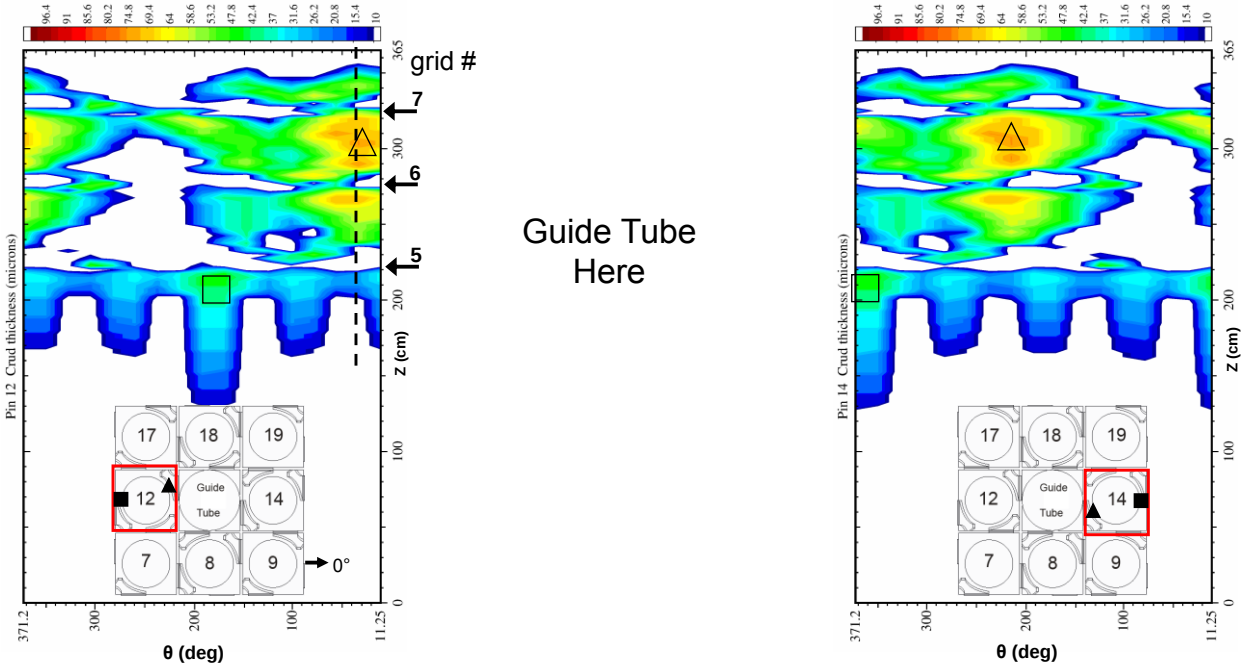

Figure 38: 2D surface contour maps of the CRUD thickness (in microns at 502 days) – pins 12 & 14. The dashed vertical line in the left panel shows the location of the 2D profile plot in Figure 40.

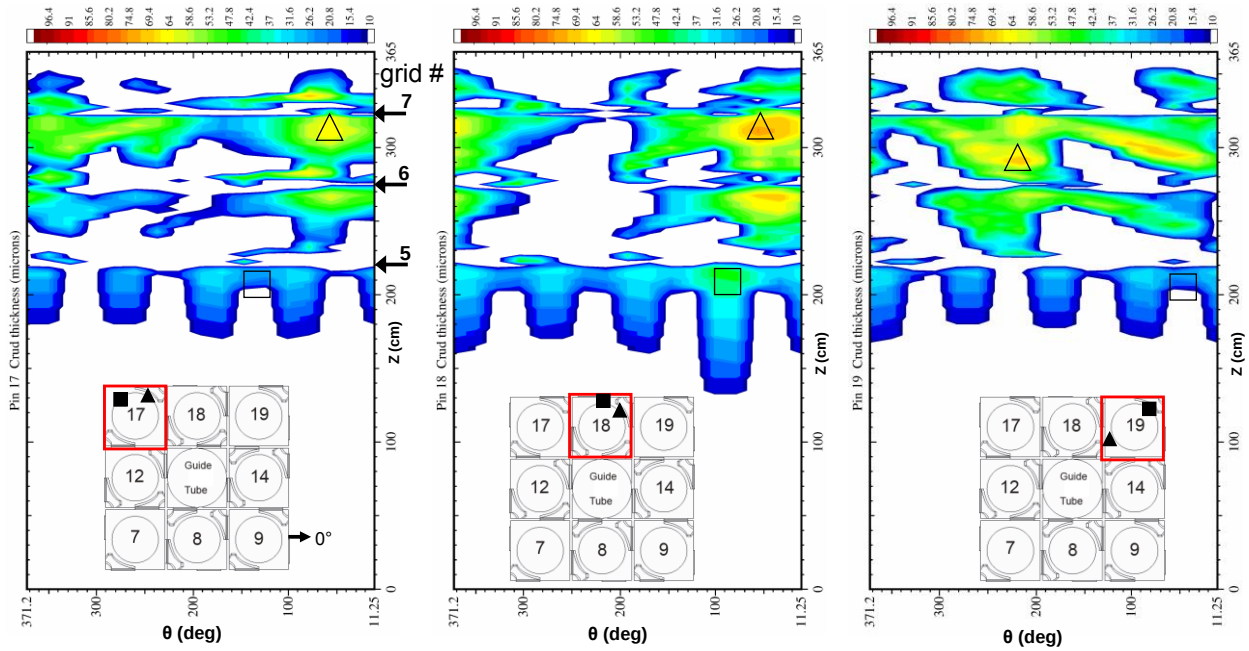

Figure 39: 2D surface contour maps of the CRUD thickness (in microns at 502 days) – pins 17 to 19.

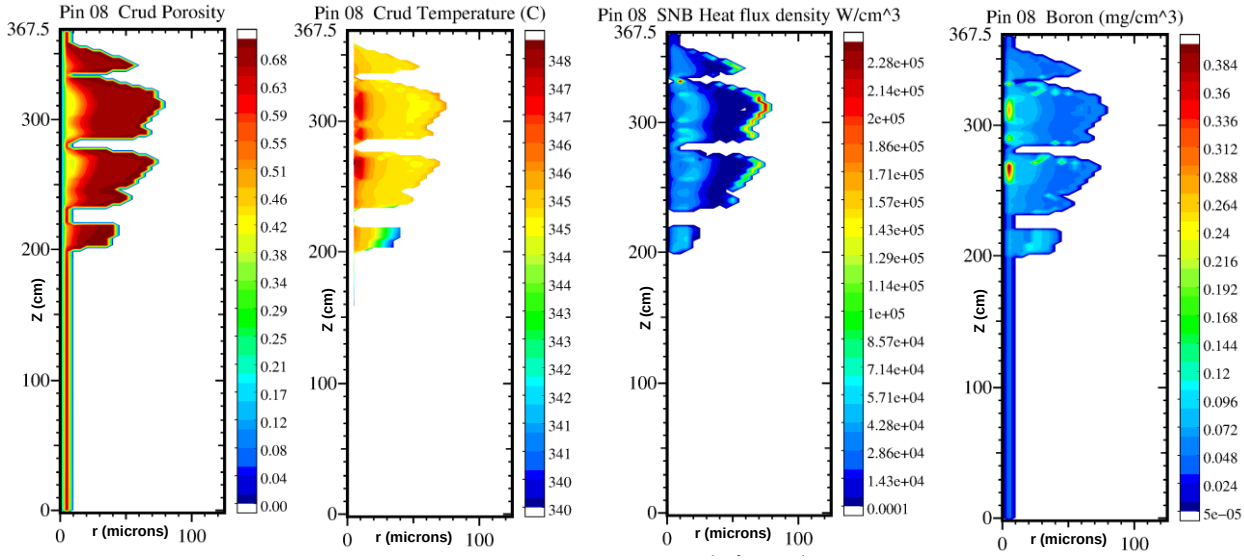

Figure 40: 2D CRUD profiles at 502 days for pin #8.

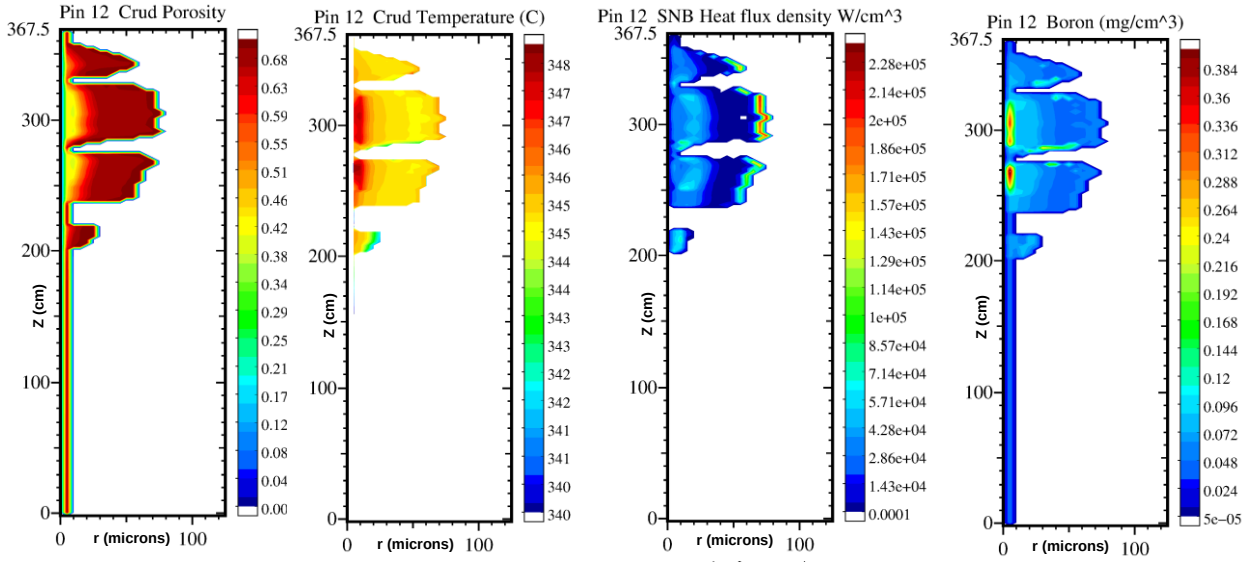

Figure 41: 2D CRUD profiles at 502 days for pin #12.

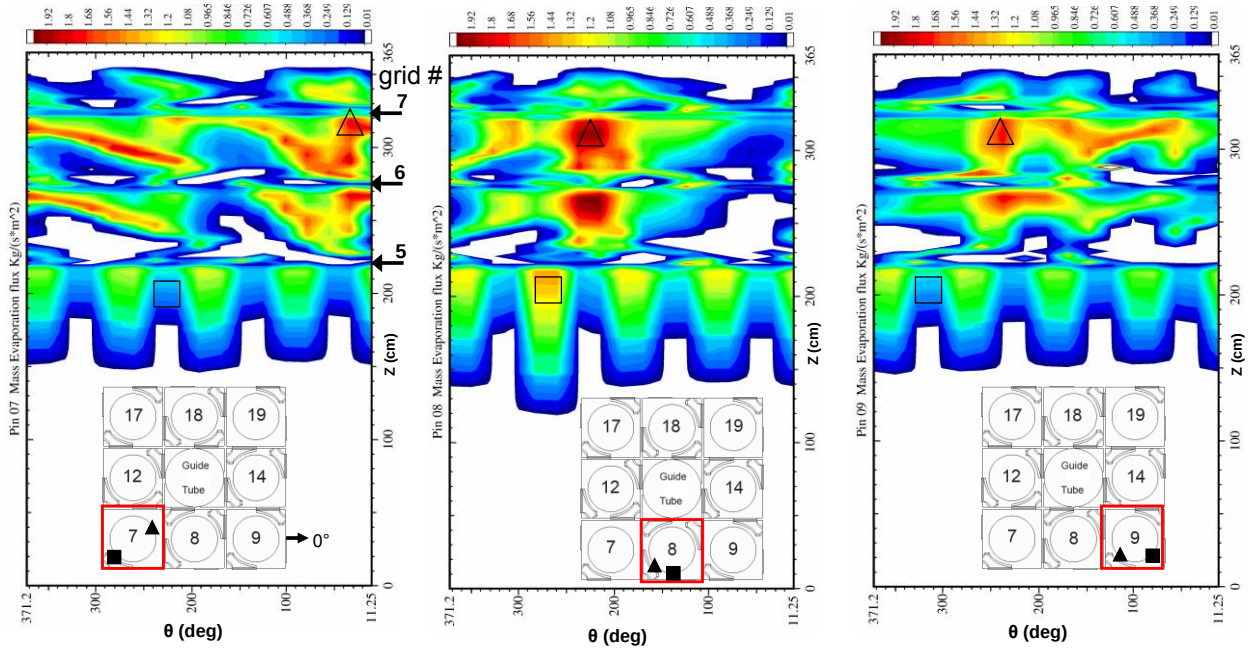

Figure 42: 2D surface contour maps of the boiling chimney mass evaporation flux [kg/s m^2] at 209 days – pins 7 to 9.

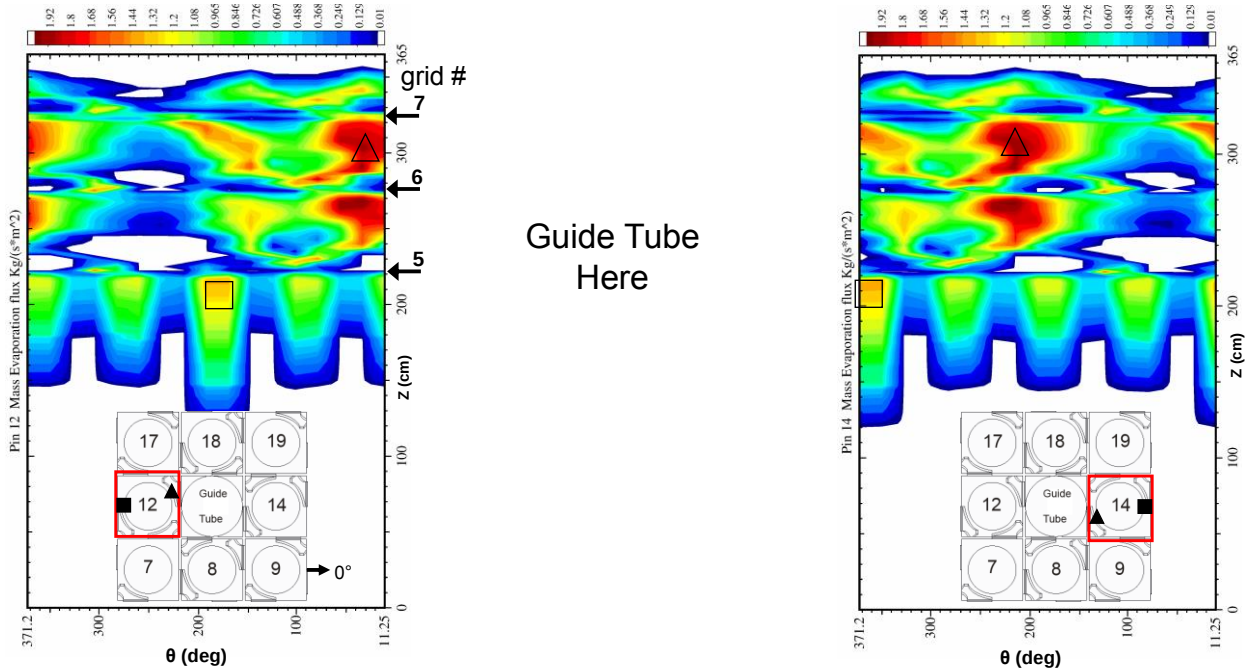

Figure 43: 2D surface contour maps of the boiling chimney mass evaporation flux [kg/s m^2] at 209 days – pins 12 to 14.

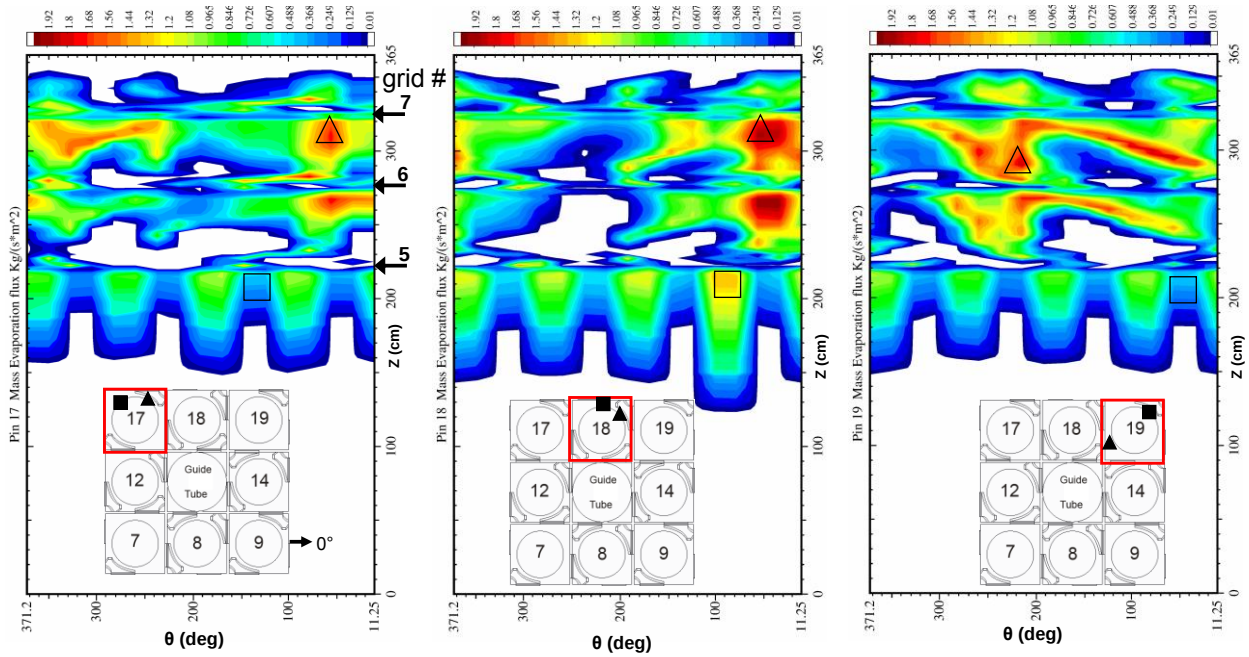

Figure 44: 2D surface contour maps of the boiling chimney mass evaporation flux [kg/s m^2] at 209 days – pins 17 to 19.

Contour plots of the mass evaporation flux due to the chimney boiling within the CRUD layer are plotted in Figure 42 to Figure 44 at day 209 (near mid-cycle when the power is largest). As expected, the regions with the highest mass evaporation rates (red) correlate directly with the regions of thicker CRUD in Figure 37 to Figure 39. The same regions of interest in Figure 37 to Figure 39 are marked in Figure 42 to Figure 44 with the open/solid triangles and squares. The strong azimuthal and axial variations due to the coolant flow are clearly visible. Since the mass evaporation flux and thick CRUD are directly correlated, mass evaporation flux maps such as those shown in Figure 42 to Figure 44 can be used to help optimize spacer grid, IFM, and mixing vane orientation designs to minimize CRUD.

3.1.2 STAR-CCM+/MAMBA with azimuthal power distribution (case 2a)

Previous work has shown that the development of CRUD is strongly influenced by the locations of "hot spots" on the cladding surface [9, 10, 12]. These locations are axially and azimuthally dependent.

In order to assess the sensitivity of the results to azimuthal power variations, the 5x5 Seabrook simulation was repeated using an azimuthally modulated ANC power profile for each rod (see Sect. 2.2.4 for details). The largest azimuthal variations where found to occur for rods #8 and 12 (and their 180° symmetric partners #14 and 18, see Figure 15).

STAR-CCM+ results (case 2a)

The cladding temperature and CRUD thickness obtained for case 2a are reported in Figure 45 and Figure 46 respectively. Small differences can be observed in the CRUD thickness when compared to the results obtained for case 1a where no azimuthal power variation is modeled. The impact of the power azimuthal variation on the cladding temperature can be better observed in Figure 47. Here the results of the azimuthal variation of the cladding temperature obtained for pin #8 in the proximity of spacer #1 are shown for case 1a (dashed lines - no azimuthal power variation) and case 2a (solid lines - with azimuthal power variation). As expected, the larger impacts of the power variation occurs around 90°, where pin #8 is facing the water rod. At this location the azimuthal power variation accounts for an increase of the cladding temperature of 2K only, while the peak-to-peak azimuthal temperature variations induced by changes in the cooling characteristics (size of subchannel or flow-swirl induced by mixing vanes) are above 15 K.

It can therefore be concluded that for CRUD-related simulations, the fidelity of the neutronics modeling is not as essential as the fidelity of the thermal-hydraulics modeling. A CFD simulation coupled with a nodal diffusion code such as ANC may be sufficient to achieve the necessary level of accuracy. On the contrary, a neutron transport simulation coupled with a subchannel code is going to miss most of the relevant thermal-hydraulics feedbacks that affect the location and evolution of the CRUD deposits. Of course, the feedback between the neutronics and the CRUD/coolant chemistry is not considered here, so further investigations should be carried out to determine the required fidelity of the neutronics model to accurately capture the feedback phenomena. For example, studies on the azimuthal power variations due to boron hideout and azimuthal neutron flux variation needed to determine local boron destruction rates should be investigated.

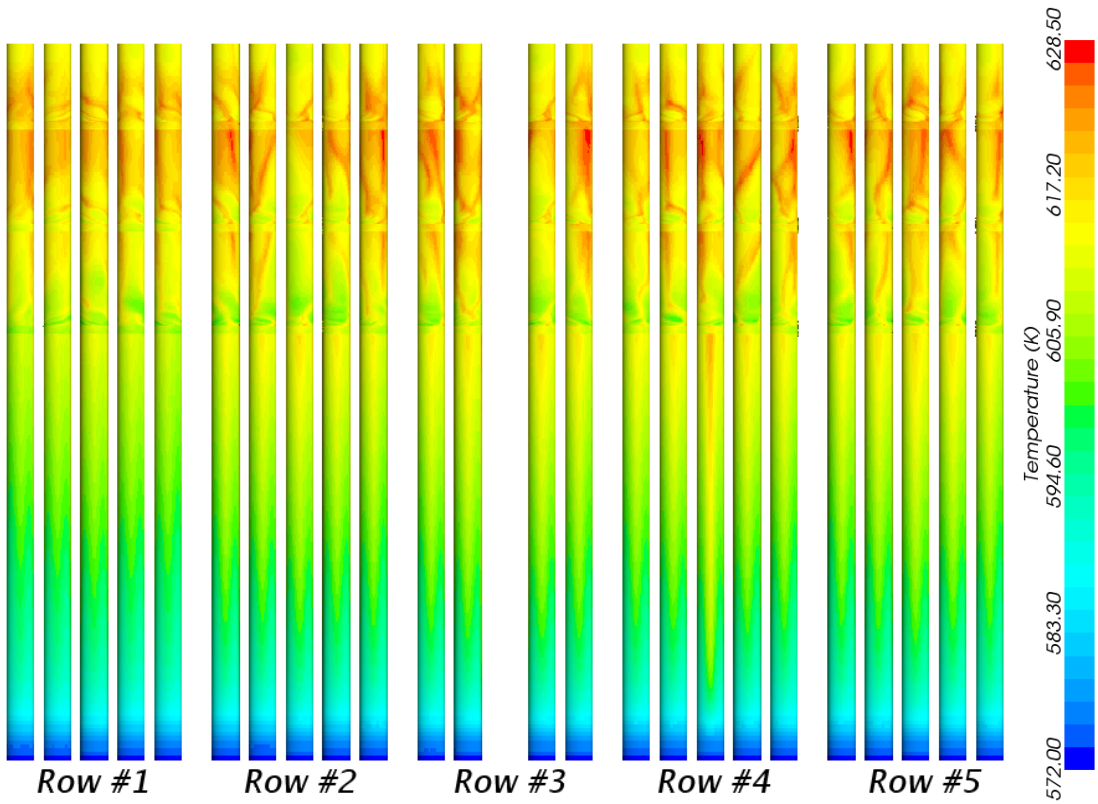

Figure 45: Cladding temperature at 502 days (case 2a).

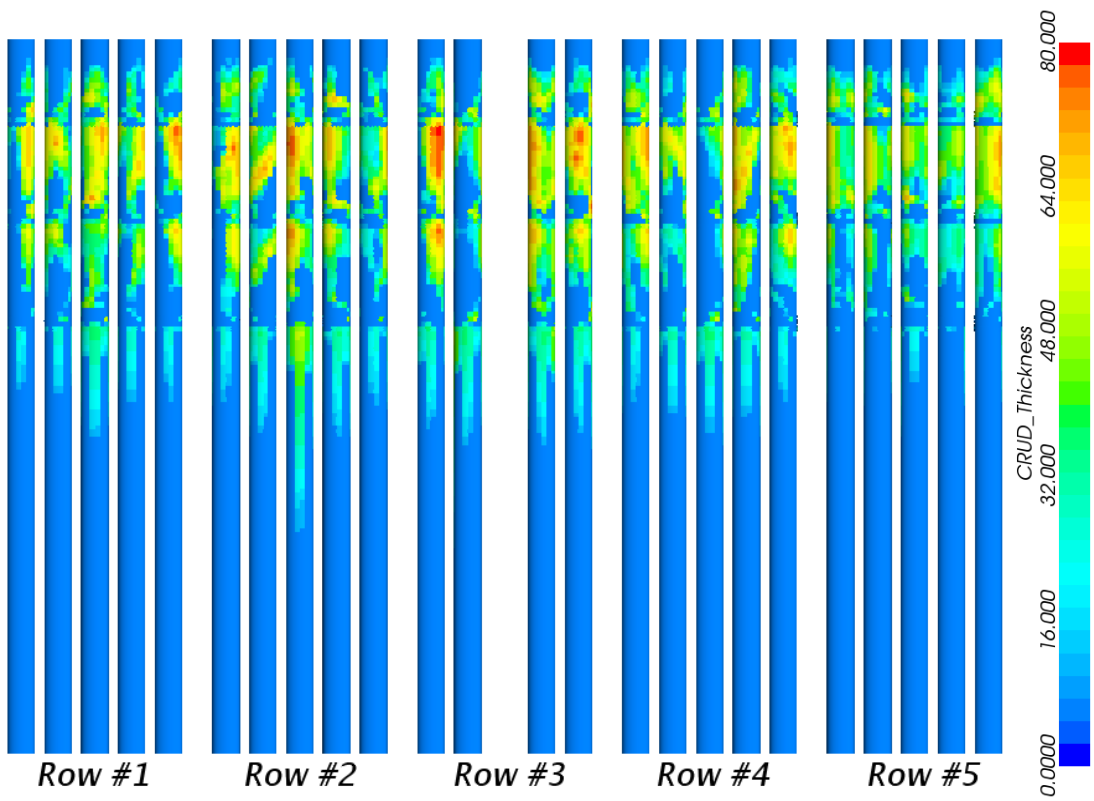

Figure 46: CRUD thickness [microns] at 502 days (case 2a).

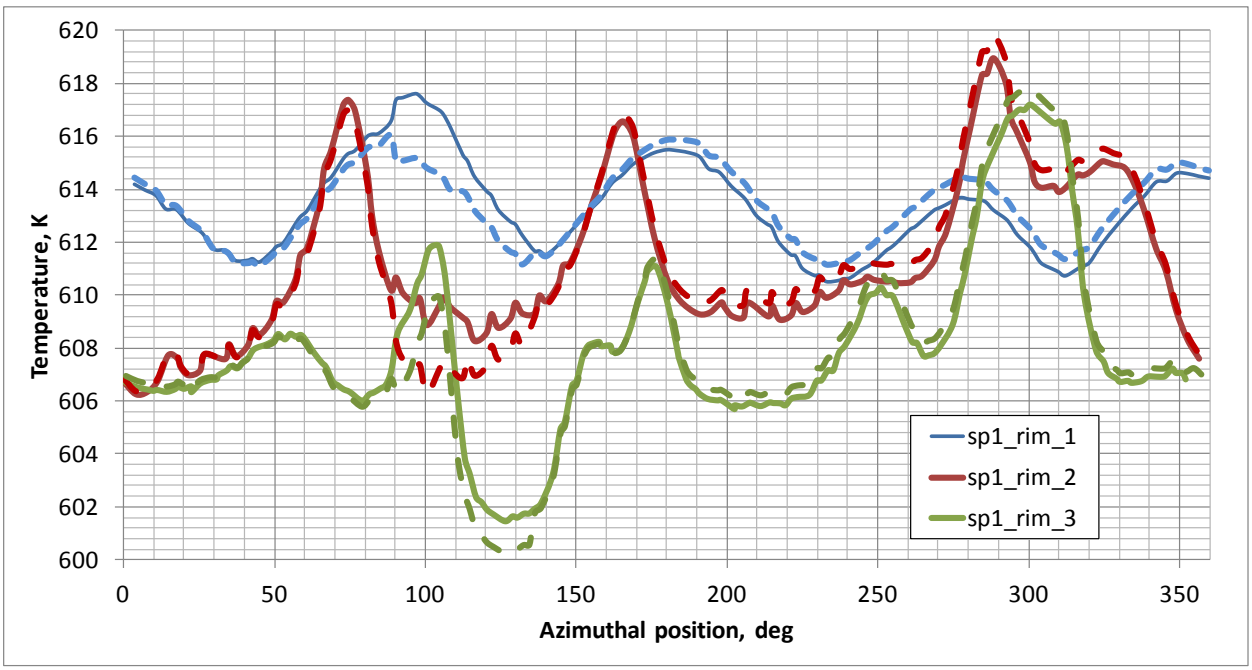

Figure 47: Azimuthal distribution of cladding temperature for pin #8, spacer 1, at 502 days. Solid lines (case 2a), dashed lines (case 1a).

MAMBA results (case 2a)

The contour plots of the CRUD thickness at the end of Seabrook cycle 5 (502 days) for rods #8 and #12 are plotted in Figure 48 and Figure 49 as a function of azimuthal angle θ (deg) and axial height z (cm). As discussed previously, these rods (and their 180° symmetric partners #14 and 18, see Figure 15) exhibit the largest azimuthal power variations.

The left-most plots in Figure 48 and Figure 49 are from the azimuthally symmetric power simulation (i.e., they are identical to the plots in Figs. 25 and 26, respectively). The center plots in Figure 48 and Figure 49 are the results using a modulated ANC power profile. The right-most plot in these two figures superimposes the contours from the symmetric and modulated simulations (for clarity only two CRUD thickness contours are plotted: 20 (black) and 60 (red) microns. The solid and dashed contours correspond to the azimuthally symmetric and modulated simulations, respectively. Small differences are observed between the two cases. The most notable effect is an increased (decreased) axial extension of the CRUD in Figure 48 in the region near θ=270° (100°). Similar behavior is observed for rod #12 in Figure 49 except in the region near θ=180° (10°). These small differences confirm that the primary effect on azimuthal CRUD deposition patterns along the surface of the rod are due to the T/H variations associated with the complex fluid flow patterns. However, additional studies using a fully coupled neutronics/CFD/CRUD framework are needed to confirm this preliminary finding. Larger azimuthal power variations could occur in a fully coupled simulation due to feedback effects between the CFD and neutronics.

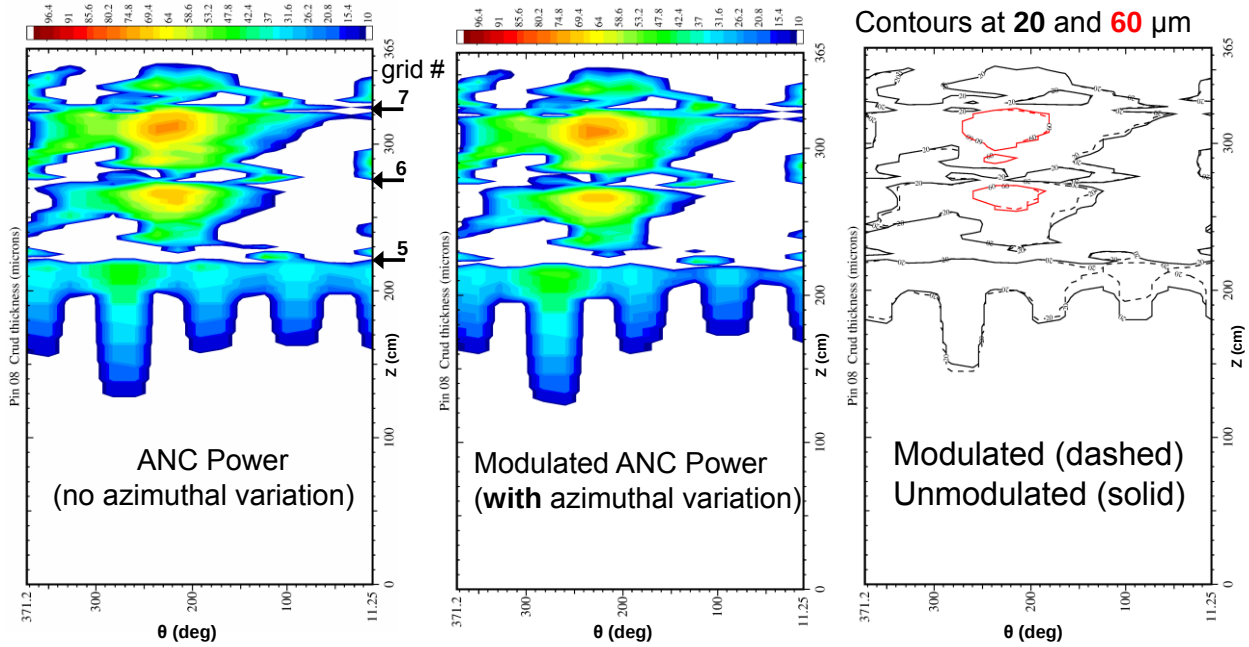

Figure 48: 2D surface contour maps of the CRUD thickness (in microns at 502 days) for pin #8 with and without azimuthal power variations.

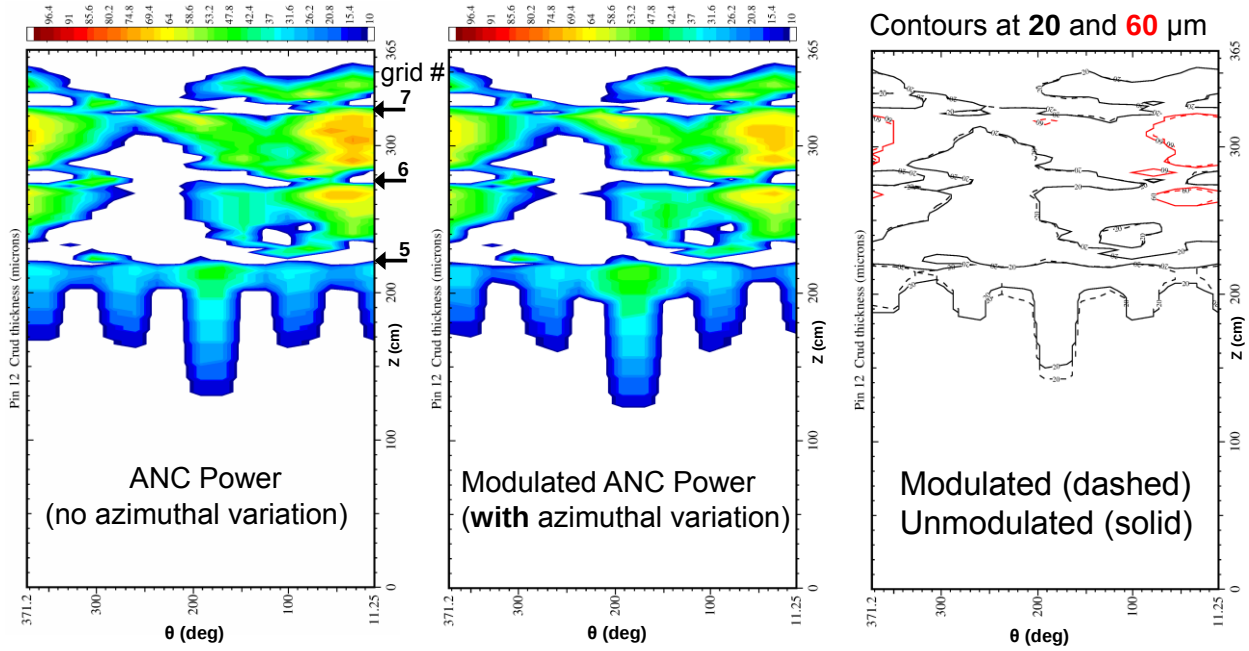

Figure 49: 2D surface contour maps of the CRUD thickness (in microns at 502 days) for pin #12 with and without azimuthal power variations.

The 5x5 depletion simulation using ANC powers with imposed azimuthal dependence showed a small increase in CRUD and boron mass. On average, a difference of approximately 0.4% by the end of the cycle occurred. Figure 50 shows the CRUD characteristics for pin 11 and 12 and Figure 51 shows the core total CRUD characteristics. It is noted that the other pins not included in Figure 50 compare similarly. As previously discussed, the azimuthal variation of the power distribution (excluding feedback to and provided by the neutronics) does not play a major role in the deposition of CRUD or the precipitation of boron.

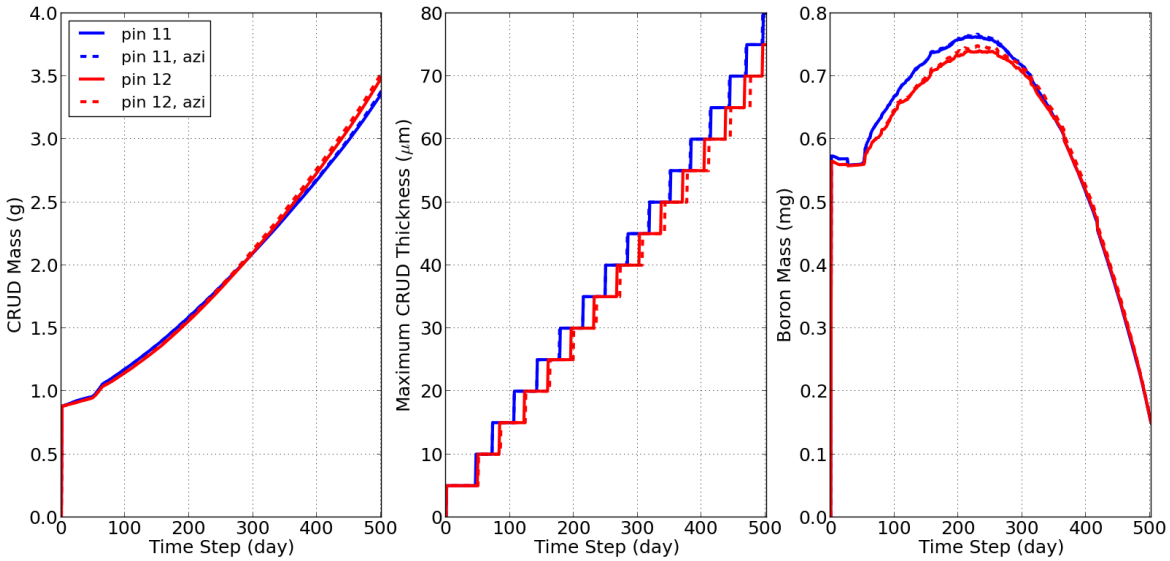

Figure 50: Integral CRUD mass, maximum CRUD thickness and integral boron mass comparison of ANC and azimuthally varying ANC power simulations for pin 11 and 12.

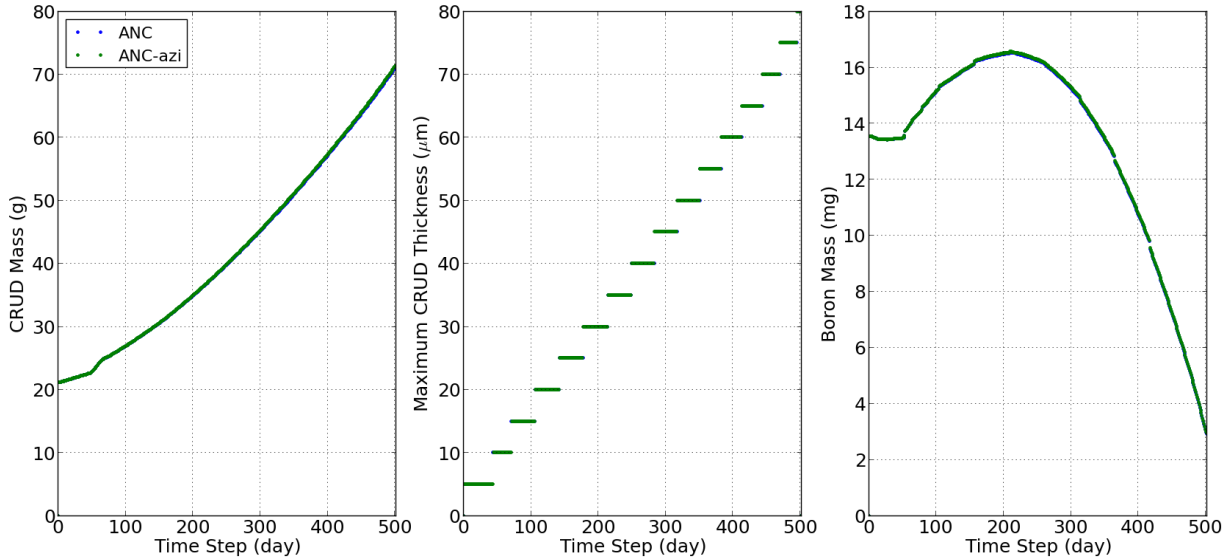

Figure 51: Core total integral CRUD mass, maximum CRUD thickness and integral boron mass comparison of ANC and azimuthally varying ANC power simulations.

3.2 RESULTS FOR SINGLE PIN TEST PROBLEM

3.2.1 STAR-CCM+/MAMBA simulations with fixed time steps (case 1b)

Time stepping and convergence sensitivity studies were performed using a single pin cell model, based on a pin cell from the Seabrook 5x5 sub-assembly. However, the pin power was slightly increased to result in precipitation of boron so that higher thermal resistances may also be studied. The time stepping study varied the frequency of data updates between MAMBA and STAR-CCM+ while performing a single MAMBA and STAR-CCM+ simulation at each time step. Figure 52 depicts the simple time stepping algorithm with a fixed power distribution provided by DeCART. Three time steps were considered, $t_{step} = 50, 25,$ and 10 days, over a cycle length of $t_{end} = 500$ days.

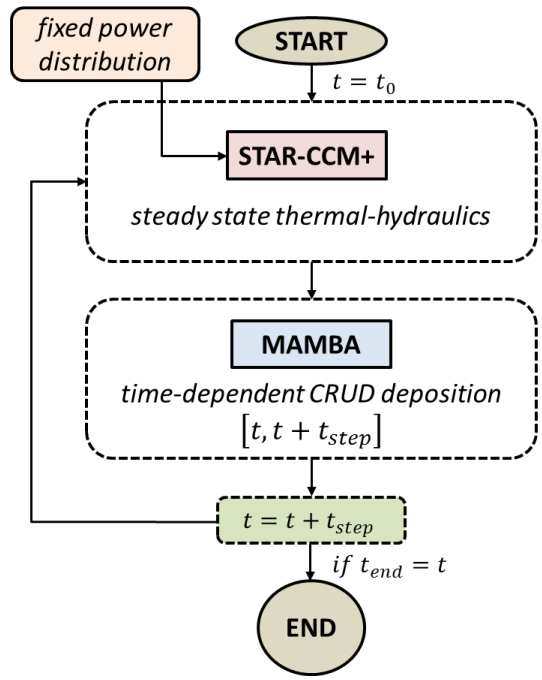

Figure 52: MAMBA/STAR-CCM+ time stepping algorithm for single pin cell time stepping study.

Figure 53 shows the CRUD and boron hideout characteristics for three different uniform time steps during the 500 day coupled simulation. In general, the CRUD mass and thickness are affected little by the time stepping.

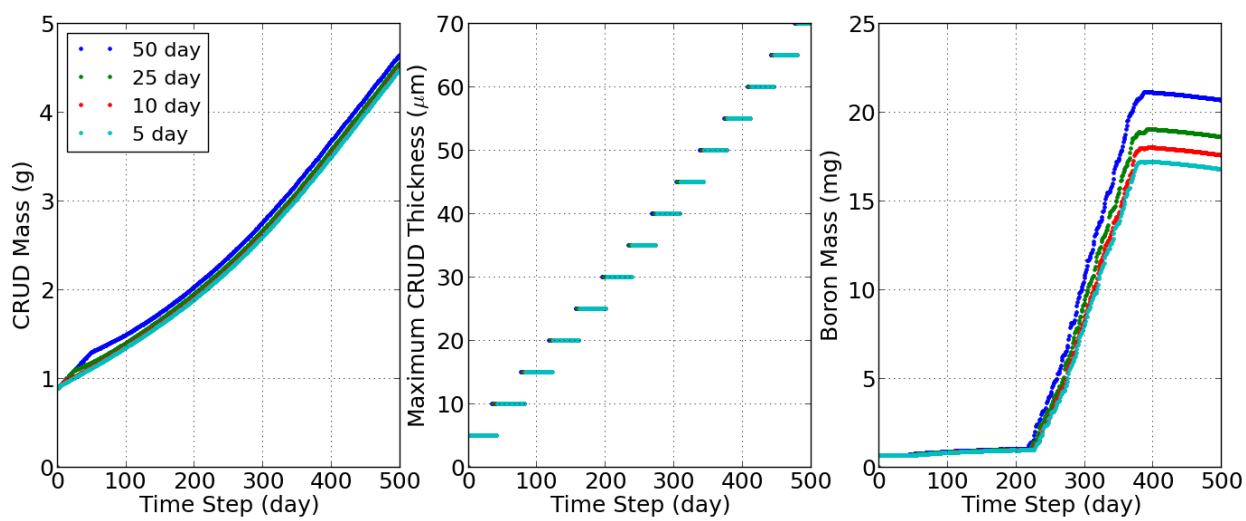

Figure 53: Integral CRUD mass, maximum CRUD thickness and integral boron mass for 50, 25, and 10 day MAMBA/STAR-CCM+ time steps (data exchanges).

However, the boron mass, which is primarily controlled by precipitation of lithium tetraborate, is much more dependent on the feedback from the thermal-hydraulics. Because the boron

precipitation behaves according to a threshold, which is controlled by species concentration and temperature, the point in time where this threshold is exceeded sensitively impacts the amount of boron that is precipitated. A relative change of approximately 10% in boron mass occurs between 50 and 25 day data updates. An additional 5% and 3.5% reduction in boron mass prediction occurs when comparing to 10 and 5 day data updates. From these results, it is concluded that to predict the CRUD mass correctly, much coarser temporal data exchanges may be performed. Nevertheless, to accurately predict the boron precipitation, data should be exchanged between thermal-hydraulics and CRUD chemistry at most every 25 days. At times where boron precipitation is not occurring, accurate predictions of the boron mass should be possible with a coarser time step.

3.2.2 Influence of turbulence model (case 2b)

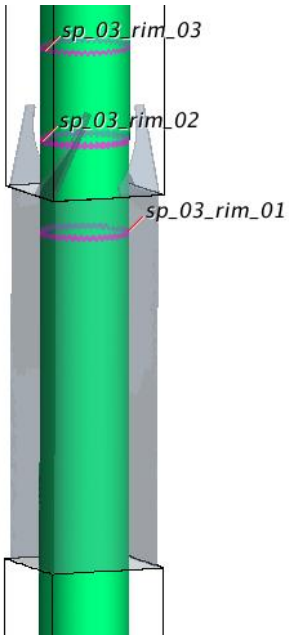

Figure 54: Axial locations in the proximity of the mixing vanes.

In order to evaluate the effect of turbulence models on CRUD build-up, a sensitivity study was performed. Because of the limited time frame available for the completion of the present milestone, this study was limited to stand-alone CFD simulations. The comparison among different turbulence models was focused on the key parameters affecting CRUD build-up and erosion: cladding temperature, turbulent kinetic energy, and wall shear stress in the proximity of the cladding surface. As for the 5x5 studies, three axial locations in the proximity of the mixing vanes are selected for comparing the models (see Figure 54). In addition, the impact of the turbulence model on the pressure drop across the third grid spacer is also investigated. The third spacer is selected because the water flow reaching this location is perturbed by the upstream spacers.

The sensitivity study presented in this chapter includes the following combinations of turbulence models and wall treatments:

- Realizable K-epsilon model [13] with high Y+ treatment
- Realizable K-epsilon two layer model [14] with all Y+ treatment
- Standard K-epsilon model [15,16] with high Y+ treatment
- Standard K-epsilon two layer model [14, 15 ,16] with all Y+ treatment
- Reynolds stress model[17]
- Quadratic K-epsilon model [18,19,20] with high Y+ treatment.

All simulations were performed using an inlet velocity of 5.278 m/s (uniform, undeveloped velocity profile), and an inlet temperature of 283.61°C. The power profile was constant and computed by means of the neutron transport code DeCART. The power distribution adopted in the simulations is shown in Figure 55. The spreading of the curve along the y-axis indicates the variation of power density along the azimuthal coordinate.

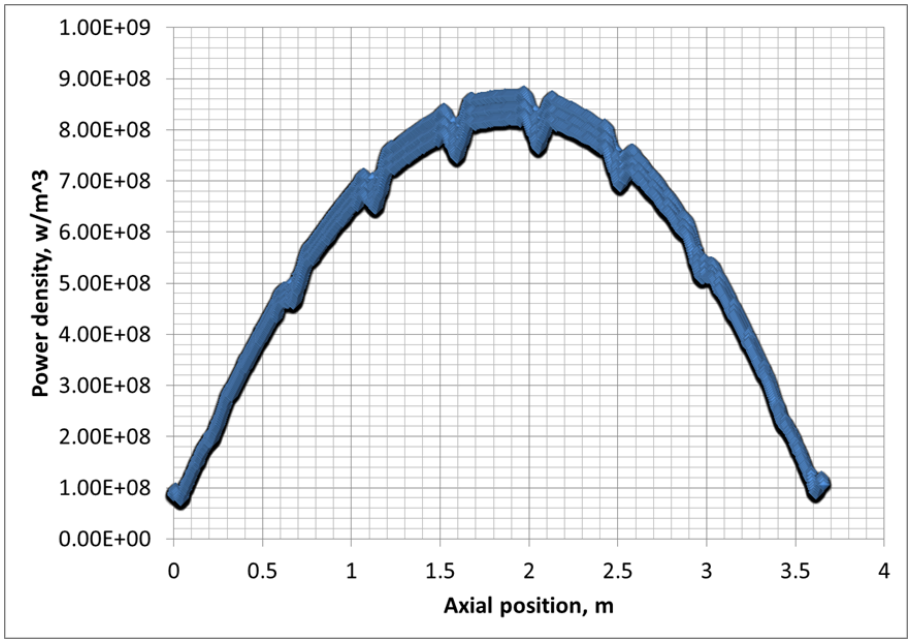

Figure 55: Power density profile used for sensitivity study 2b.

Table 9 – STAR-CCM+ mesh information for single-pin model.

Model	Pressure drop [Pa]	Deviation
Relz. K-eps. High Y+	22737	-0.027
Relz. K-eps. two layer All Y+	22701	-0.029
Std. K-eps. High Y+	23403	0.001
Std. K-eps. two layer All Y+	23378	0.000
RSM High Y+	23619	0.010
Quad. K-eps. High Y+	23132	-0.011

The values of the pressure drops across grid spacer #3 obtained with the different turbulence models are listed in Table 9. Here the deviations are given taking the standard k-epsilon two-layer model with all Y+ treatment as reference. As shown in Table 9, the highest deviations in pressure drop fall in the range of -2.9% to 1% and are obtained when the realizable k-epsilon model is employed.

It is worth mentioning that we have found that realizable k-epsilon models tend to exhibit flow oscillations (i.e. steady-state solution does not exist) when applied to relatively tight-lattice bundles without spacers. Because of these flow oscillations, the CFD simulations when a realizable k-epsilon model is applied, needs to be executed in “transient mode”, rather than as steady-state, yielding significantly higher computational costs. Because the 5x5 sub-assembly and single pin cell CFD models used in the present work do not contain spacers or mixing vanes in the lower half of the core, flow oscillations were prone to develop when the realizable k-epsilon model was employed. It should also be mentioned that recent studies have shown that the realizable k-epsilon model may provide a noticeable pressure drop discrepancy with respect to experiments [21]. Therefore, this type of model is not recommended for the bundle and single-pin applications discussed in the present report.

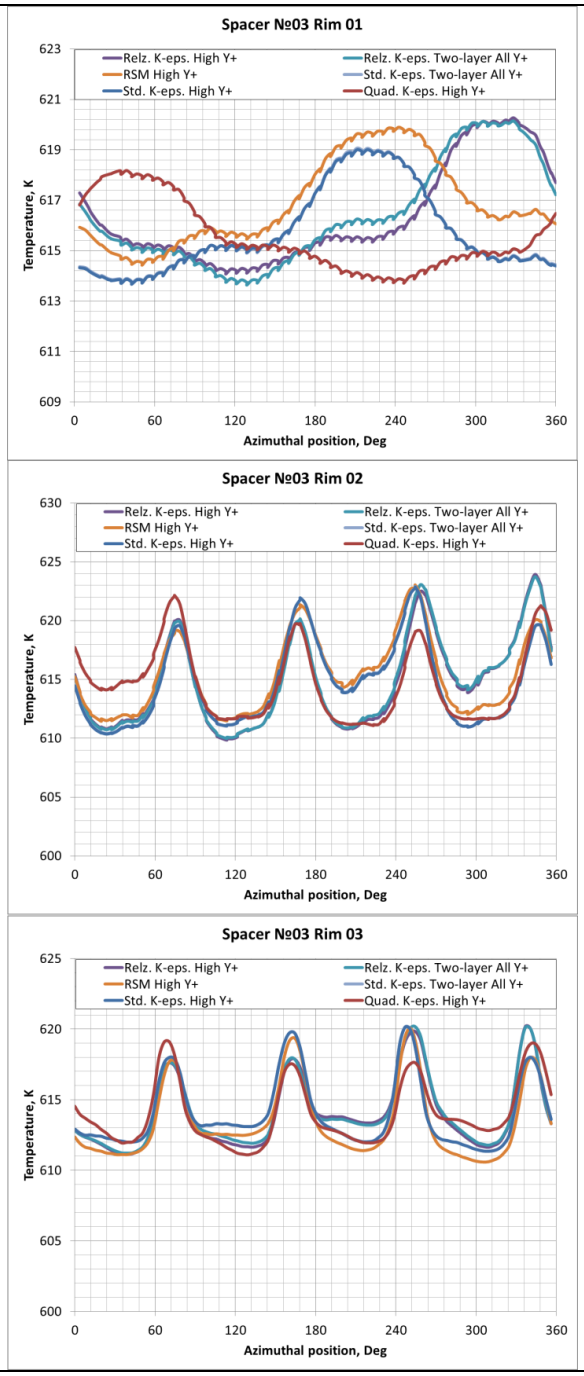

Figure 56: Azimuthal variation of cladding temperature in proximity of grid spacer #3.

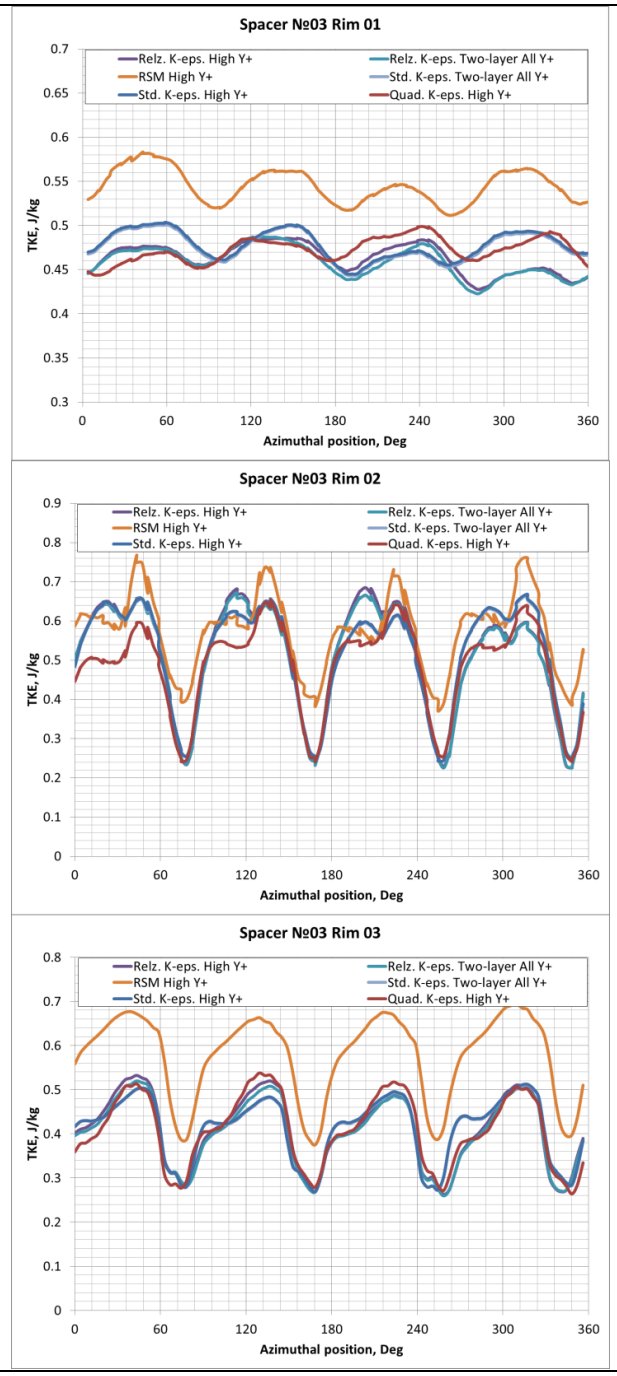

Figure 57: Azimuthal variation of turbulent kinetic energy in proximity of grid spacer #3.

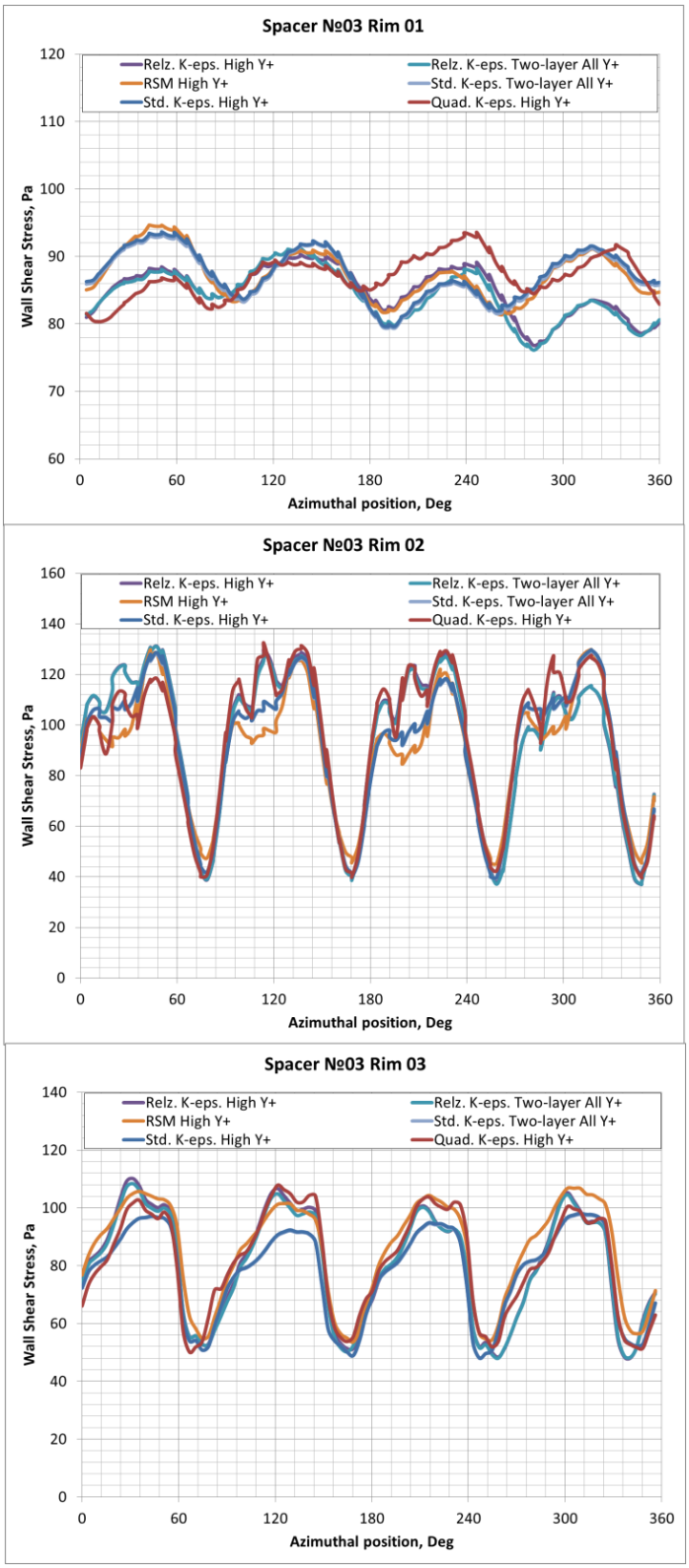

Figure 58: Azimuthal variation of turbulent kinetic energy in proximity of grid spacer #359.

The use of high Y+ wall treatment is limited by the fact that these types of models require a Y+ higher than 30, which is challenging to achieve because of the small gaps formed where the grid spacers are located. In these cases, small gaps might be meshed too coarsely. The Reynolds stress model is significantly more computationally expensive because it involves the solution of additional partial differential equations for the Reynolds stresses. The quadratic k-epsilon model appeared to be numerically unstable and required extra measures such as adjustments of the under-relaxation parameters. The azimuthal variations of cladding temperature, turbulent kinetic energy and wall shear stress in the proximity of spacer #3 are reported in Figure 56 to Figure 58 respectively, as obtained with the turbulence models listed in Table 9. Overall all turbulence models exhibit similar behavior with respect to TKE and shear stress profiles, with the exception of the Reynolds stress model for which the TKE has higher values and the cladding temperature for rim 1 has a smaller range of variations. In order to better understand this discrepancy, an additional investigation would be required aimed at evaluating the impact of the Reynolds stress model constants. The difference among the various turbulence models will reduce when applied to models larger than the single-pin treated in this sensitivity study (e.g., 5x5 sub-assembly), because the effect of the boundary conditions on the subchannel flow will be mitigated in a larger domain. The largest differences among the turbulence models predictions are observed for the cladding temperature profiles in rim 1 (see Figure 56, top), upstream of the mixing vanes. The reason for this is that in this region, the flow is completely surrounded by the spacer walls and the effect of secondary of secondary motions is more dominant.

4 CONCLUSIONS

In summary, two coupled STAR-CCM+ / MAMBA simulations were performed for a 5x5 subassembly from fuel assembly G70 in Seabrook cycle 5. An imposed power distribution from the WEC ANC neutronics code was used to set the individual pin powers within the 5x5 at 13 depletion steps during the 502 day cycle. The first coupled 5x5 simulation used the azimuthally symmetric ANC power distributions (case 1a). The second coupled 5x5 simulation used a azimuthally modulated ANC power distribution (case 2a). The azimuthal dependence was computed by DeCART. The resulting CRUD distributions for both of these simulations were nearly identical which showed that the thermal hydraulic effects dominate in this case. The imposed azimuthal power variations had little effect on the CRUD deposits. Thus, the fidelity of the neutronics modeling is not as essential as the fidelity of the thermal-hydraulics modeling since the impact of the azimuthal power variation on the core-wide CRUD and boron mass is negligible. As a matter of fact, it has been found that, despite up to 3% variations in the power density around the fuel rod, the resulting effects on the build-up of CRUD were less than 0.4%. It can therefore be concluded that a CFD simulation coupled with a nodal diffusion code such as ANC can be sufficient to achieve the necessary level of accuracy. On the contrary, a neutron transport simulation coupled with a subchannel code is going to miss most of the relevant thermal-hydraulics feedbacks that affect the location and evolution of the CRUD deposits. Of course, the feedback between the neutronics and the CRUD/coolant chemistry is not considered here, so further investigations should be carried out to determine the required fidelity of the neutronics model to accurately capture the feedback phenomena. Explicit feedback from neutronics is not included in this work because the ANC power distributions were pre-computed and did not depend on the thermal-hydraulic and CRUD predictions.

From the single pin time stepping study it has been concluded that to accurately capture the physics of boron precipitation, temporal data exchanges of 25 days or less are required. Data exchanges every 5-10 days would be preferable because the difference in predicted boron mass between 50 and 5 days is nearly 20%. However, the CRUD mass and boron mass (excluding times of precipitation) are accurately predicted using data exchanges every 50 days. Extended exchange intervals (>50 days) may also be acceptable but were not investigated in this study.

From the single pin turbulence model studies, we do not expect the particular choice of turbulence modeling to significantly affect the prediction of CRUD build-up, the only exception being the Reynolds stress turbulence model. This model however it is not recommended for fuel bundle applications since the coefficients of the models have not been optimized for this type of geometry.

Initial comparisons of our 5x5 CRUD predictions with the Seabrook CRUD data were also performed for pin G09 (our pin #8) from fuel assembly G70. These initial comparisons are encouraging despite the discovery of several differences in geometry, such as: mixing van orientation, spacer grid location, and spacer grid width. The comparisons further confirm the importance of thermal hydraulic effects (i.e., due to mixing vane orientation) and the need for a high-fidelity coupled CFD/CRUD chemistry modeling approach. The favorable comparisons with the Seabrook data are also encouraging in that no model parameters were adjusted and the calculations were completed before the data became available. A more detailed summary of the Seabrook comparisons is given in Chapter 6.

FUTURE WORK

In future work, a coupled neutronics/CFD/CRUD simulation for the same 5x5 with corrected geometries will be performed in order to accurately assess all of the feedback effects. A coupled simulation between all three codes will determine the relative importance of the various feedback phenomena. This insight will be crucial for guiding the development and coupling of codes with the proper fidelity. The current study focused on CILC effects. Future studies will also focus on boron uptake and the conditions required for significant precipitation of boron species. The CRUD is likely to be thicker on the interior rods of a fuel assembly which could lead to a significant increase in boron uptake. Additional 5x5 simulations will be pursued with an increased CRUD deposition rate to investigate the effects of thicker CRUD. Future work also includes investigation of a fixed-point Gauss-Seidel iteration between STAR-CCM+ and MAMBA at each depletion step. Additional turbulence model studies will also be pursued in conjunction with the development of improved CRUD erosion models. Improved grid mapping routines based on conservative interpolation methods will also be investigated.

ACKNOWLEDGEMENTS

We thank Dennis Hussey, Chris Stanek, Jeff Secker, and Zeses Karoutas for their help and support in defining the work scope and execution plan for this L2 milestone. We also thank Jeff and Zeses for their help in defining a representative non-proprietary geometry model for the spacer grids. We thank Jeff Deshon for providing additional information on the Seabrook cycle 5 coolant chemistry.

5 REFERENCES

1. Boyd, W.A., Mayhue, L.T., Penkrot, V.S., Zhang, B., 2009. The WhiteStar development project: Westinghouse's next generation core design simulator and core monitoring software to power the nuclear renaissance. Proc. of Int. Conf. on Mathematics, Computational Methods & Reactor Physics (M&C 2009), Saratoga Springs, New York, May 3 – 7.
2. Seabrook cycle 5 report from WEC to CASL: CE-11-285 and CE-11-198, Rev 1 in support of CASL AMA milestone: AMA.CHALNG.07.Y1, March 29, 2011.
3. Hursin, M., Kochunas, B., Downar, T., 2008. DeCART v2.05 Theory Manual.
4. Navarro, M.A., Santos, A.A.C., 2011. Evaluation of a numeric procedure for flow simulation of a 5x5 PWR rod bundle with a mixing vane spacer, Progress of Nuclear Energy, 53, pp. 1190-1196.
5. Karoutas, Z.E., Lu, R., Yan, J., Krammen, M.A., Sham, T.-L., 2012. Application of advanced methods to predict grid to rod fretting in PWRs.
6. CASL, 2012. Vera Benchmark Problems.
7. Petrov, V., Manera, A., 2012. AMA/THM Memorandum - Non-proprietary Fuel Assembly geometry specifications for CFD applications, May 24.
8. Email correspondence with Jeff Secker and Jeff Deshon, August 21, 2013.
9. Walter, D., Collins, B., Kendrick, B., Petrov, V., Manera, A., Downar, T., 2013. High-fidelity simulation of CRUD deposition on a fuel pin with grid spacers - a proof-of-principle using the fully coupled MAMBA/DeCART/STAR-CCM+ code. Proc. of NURETH-14 conference, Pisa, Italy, May 12 - 16.
10. Petrov, V., Kendrick, B., Walter, D., Manera, A., 2013. Impact of fluid-dynamic 3D spatial effects on the prediction of CRUD deposition in a 4x4 PWR sub-assembly. Proc. of NURETH-14 conference, Pisa, Italy, May 12 - 16.
11. Kendrick, B. K., Barber, J., 2012. Initial validation and benchmark study of 3D MAMBA v2.0 against the WALT loop experiment and BOA v3.0. CASL report MPOCRUD.P5.02, August 10.
12. Kendrick, B., Walter, D., Petrov, V., Manera, A., Downar, T., 2011. Proof-of-concept of Decart/STAR-CCM+/MAMBA coupled simulation for the prediction of CRUD deposition on a fuel pin with grid spacers. L1.CASL.P4.02
13. Shih, T.-H., Liou, W.W., Shabbir, A., Yang, Z. and Zhu, J., 1994. A New k- Eddy Viscosity Model for High Reynolds Number Turbulent Flows -- Model Development and Validation. NASA TM 106721.
14. Rodi, W., 1991. Experience with Two-Layer Models Combining the k-e Model with a One-Equation Model Near the Wall", 29th Aerospace Sciences Meeting, January 7-10, Reno, NV, AIAA 91-0216.
15. Jones, W.P., Launder, B.E., 1972. The Prediction of Laminarization with a Two-Equation Model of Turbulence. Int. J. Heat and Mass Transfer, 15, pp. 301-314.

16. Launder, B.E., Sharma, B.I., 1974. Application of the Energy Dissipation Model of Turbulence to the Calculation of Flow Near a Spinning Disc. Letter in Heat and Mass Transfer, vol. 1, no. 2, pp 131-138.

17. Gibson, M.M., Launder, B.E., 1978. Ground effects on pressure fluctuations in the atmospheric boundary layer, J. Fluid Mech., 86(3), pp. 491-511.

18. Lien, F.S., Chen, W.L., Leschziner, M.A., 1996. Low-Reynolds number eddy-viscosity modelling based on non-linear stress-strain/vorticity relations. Proc. 3rd Symp. on Engineering Turbulence Modelling and Measurements, 27-29 May, Crete, Greece.

19. Baglietto, E., Ninokata, H., Misawa, T., 2006. CFD and DNS methodologies development for fuel bundle simulations, Nuclear Engineering and Design, 236, pp. 1503-1510.

20. Shih, T.-H., Zhu, J., Lumley, J. L., 1993. A realizable Reynolds stress algebraic equation model, NASA TM 105993.

21. Sugrue R., Conner M., Yan J., Baglietto E., 2013. Pressure drop measurements and CFD predictions for PWR structural grids. Proceedings of TopFuel 2013 conference, Charlotte, North Carolina, September 15-19.